

Met O 11 Technical Note No 161

(Supersedes Tech Note No 157)

A Study of the Structure of Mid-Latitude Depressions
in a Numerical Model using Trajectory Techniques
I Development of Ideal Baroclinic Waves
in Dry and Moist Atmospheres

by

B Golding

Meteorological Office (Met O 11)
London Road
Bracknell
Berkshire
England
August 1982

NB This paper has not been published. Permission to quote from it must be obtained from the Assistant Director of the above Meteorological Office Branch.

A Study of the Structure of Mid-latitude Depressions in a Numerical Model using Trajectory Techniques. I. Development of Ideal Baroclinic Waves in Dry and Moist Atmospheres.

by

B. Golding

SUMMARY

Trajectory tracing techniques are used to investigate the structure and air flow of developing baroclinic waves simulated by a numerical atmospheric forecast model. Three stages are described. The structure of the linear stage is explained with reference to the normal mode theory of baroclinic instability. In the mature stage, flow separation zones form which are identified as warm and cold fronts. At the occluded stage, circulation of cold air round the centre of the depression leads to changes in the structure of the cold front. When the initial state is nearly saturated, the overall development is speeded up, and at the mature stage the rate of deepening of the depression is doubled at the surface. In the occluded stage formation of a warm air conveyor belt is observed. Comparisons are made with previously published integrations by specially constructed models in order to establish a basis for comparison of forecasts from real data which will appear in a future paper.

1. INTRODUCTION

The work described in this paper forms part of an attempt to relate the observed features of mid-latitude depressions to the theory of baroclinic wave development. A future paper will describe the application of techniques described here to integrations from real initial states.

The theory of baroclinic waves was established in the papers of Eady (1949) and Charney (1947) using a perturbation analysis of the quasi-geostrophic equations. The instability in the solution was interpreted as a wave which drew energy from the thermal gradient of the initial state. The resultant eddies were tentatively identified with the familiar depressions of the mid-latitude westerlies despite exhibiting none of the synoptic scale weather features associated with such systems. The theory has advanced in many directions since then. Basic states other than a uniform jet on an f plane have been investigated (Green 1960, McIntyre 1970, Simmons & Hoskins 1976). Work has also been published on the non-linear development of the waves using both analytical (Pedlosky 1970) and numerical techniques (Mudrick 1974). It can be shown that the quasi-geostrophic approximation becomes locally invalid as the non-linear development proceeds. The understanding of these processes has been increased by use of the semi-geostrophic equations (Hoskins & Bretherton 1972, Hoskins 1975, Hoskins & West 1979).

Observational studies of mid-latitude depressions have a longer history and started as soon as the exchange of simultaneous weather observations was made possible by the invention of the telegraph. The Bergen school (Bjerknes 1918, Bjerknes & Solberg 1922) established a synoptic scale description of the structure of depressions and this

was altered in detail only by the advent of regular upper air soundings. More recent studies have concentrated on the meso-scale structure of parts of depressions rather than the overall structure of the whole system.

The object of the present study is to try to fill some of the gaps separating these two branches of study. The work is based on a numerical model designed for routine weather forecasting. There are inherent weaknesses in this approach. The model grid-length is too large to represent many features observed in detailed studies of real depressions. However, it is well established that such models can reproduce observed synoptic scale features. A forecast model includes smoothing processes which keep it stable in real forecasts but, which may obscure the details of baroclinic wave development in idealised studies. Also, as a result of using the primitive equations, a number of different processes will be represented by the model which may not be much easier to separate in the model solutions than they are in observational data. Thus there is a need to relate the forecast model results to theoretical studies based on specially constructed models. By doing this, the ability of the forecast model to reproduce the theoretical results can be established. At the same time, a link can be made between the forecast model behaviour and a hierarchy of research results relating recent theoretical models to simpler models and ultimately to the linear instability problem. Once this link has been made, the forecast model results for real situations may be related to those for the idealised situation.

An important element in the behaviour of real depressions is the influence of moisture. In order to relate studies of real depressions

to the ideal baroclinic wave development, it is useful to understand the influence of latent heat release. This can be assessed by comparing the evolution of the ideal baroclinic wave in dry and moist atmospheres. The moisture integration presented here used an initial humidity of 90%.

The main tool for analysing the structure of depressions in the present work is the calculation of air parcel trajectories. Trajectory computation has been used as an analytical technique for some time. Djuric (1961) demonstrated the application of computers to the problem and concluded that gaps in the observational network were the main hindrance to accurate computation. Danielson (1961) also investigated the accuracy of trajectory calculations and demonstrated the benefits of isentropic analysis as a way of computing vertical motions. These techniques were extended by Green, Ludlam & McIlveen (1966) who described the circulation in mid-latitude depressions by a simple consideration of isentropic trajectories. Difficulties remained with the technique, however, due to the poor space and time resolution of the observing network. In field experiments such as that reported in Browning & Harrold (1969), considerable use is made of the assumption of stationarity in the depression's structure in order to use frequent observations at a single location to obtain an isentropic analysis from which to compute trajectories. This assumption is rarely justified except as a first approximation. Numerical models have considerable advantages over observations in this respect. Not only are the data available on a regular grid at frequent intervals, but they are self consistent and do not suffer from aliasing problems since small scale features cannot be represented in the model. An example of trajectory computations for a depression in a general circulation model was given

by Gilchrist (1971). The consistent specification of vertical velocity in numerical models removes the need to use isentropic coordinates to obtain three dimensional trajectories and has the advantage of dealing adequately with large scale diabatic sources. The remaining source of error, apart from that in the forecast itself, lies in the sub grid-scale mixing processes, primarily convection. In this paper it will be demonstrated that trajectories provide a useful means for analysing the non-linear development of a baroclinic wave, particularly in the frontal regions.

2. TECHNIQUES

The numerical forecast model used for the studies was the Meteorological Office Operational Model (Burridge & Gadd 1977, Gadd 1978a, 1978b, 1980). It is a pressure coordinate model with 10 equally spaced levels at 100 mb intervals. The horizontal grid is defined on a polar stereographic projection of the earth's surface. For the ideal baroclinic wave integration, the coarse mesh 'Octagon' version was used which has a grid length of 300 Km at 60°N and covers most of the Northern Hemisphere north of 20°N. The grid is staggered with horizontal velocity components at the centre of each grid square and vertical velocity at mid-level. The split explicit time integration scheme (Gadd 1978a) was used with a time step of 30 mins. Orography was set to zero everywhere and all physical processes were removed except horizontal diffusion and a convective adjustment procedure which are needed to preserve stability. In the moist run, a large scale condensation routine was included to provide the necessary latent heat release. This included re-evaporation of falling rain and, where

appropriate, modelling of the ice phase. No surface moisture flux was included so the total moisture in the model will have decreased once rainfall started.

The model was integrated for 7 days and values of height and velocity were output at every grid point and level each hour. The velocity components were interpolated to trajectory locations directly from their staggered grid positions to avoid unnecessary smoothing. The interpolation was linear in the three coordinate directions. Integration of the trajectory equation was performed using the following algorithm

$$\begin{aligned} \tilde{x}^{n+\frac{1}{2}} &= \tilde{x}^n + \underline{u}^n(\tilde{x}^n) \cdot \frac{\Delta t}{2} \\ \tilde{x}^{n+1} &= \tilde{x}^n + \underline{u}^{n+\frac{1}{2}}(\tilde{x}^{n+\frac{1}{2}}) \cdot \Delta t \end{aligned} \quad (1)$$

where \tilde{x} is position, $\underline{u}(\tilde{x})$ is the interpolated model velocity at position \tilde{x} and n is the time level. Since \underline{u} was available from the model every hour, a new position \tilde{x} was obtained every two hours. Diagnostic quantities such as vorticity and temperature were produced in map form for a part of the forecast domain and were also interpolated to trajectory positions. Details of the calculation of these quantities may be found in Golding (1981).

Checks were performed to verify that the trajectories gave a true representation of the air flow simulated by the model. No significant difference was found when the timestep was halved by obtaining data from the forecast model every 30 mins. Results obtained using the model velocities in Eq 1 were compared with others obtained from the

model height field using the Lagrangian form of the momentum equation to predict \underline{u}

$$\frac{d\underline{u}}{dt} = -\hat{k} \wedge \underline{u} - g \nabla h + \text{map projection terms} \quad (2)$$

Again the results were similar, but rather rougher especially in frontal regions. No significant difference in mean path could be seen and since the roughness made the results more difficult to interpret, the use of model velocities in Eq 1 was preferred. Conservation of potential temperature by individual parcels was satisfied within the error of interpolation from mean layer temperatures, except by a few parcels in frontal regions at the occluding stage. By contrast, the vorticity equation

$$\frac{d(\zeta+f)}{dt} = -\mathcal{D}(\zeta+f) - \left(\frac{\partial v}{\partial p} \frac{\partial \omega}{\partial x} - \frac{\partial u}{\partial p} \frac{\partial \omega}{\partial y} \right) \quad (3)$$

where ζ is relative vorticity and \mathcal{D} is divergence, was poorly satisfied. The error could not be explained by diffusion or minor map projection corrections. Eventually, it was found that the model integration scheme performs a considerable smoothing on the divergence term. Details of the analysis are given in the Appendix but rough calculation shows that the size of this term could be reduced by half in frontal regions. This explains the discrepancy in the trajectory results and is also the most likely reason for the low maximum vorticities found at the mature and occluding stages compared with those obtained by Hoskins & West (1979).

In order to look at the stages of development of the wave, trajectories were computed for 48 hour periods starting at several times

in the forecast. In each case an initially square grid of air parcels was started at two levels (750 mb and 950 mb) and the subsequent motion displayed relative to the movement of the surface low pressure centre. The trajectories are displayed by plotting the positions as a series of crosses where size varies linearly with pressure and is zero 100 mb below the starting level. (No parcels descended more than 100 mb in 48 hours). A selection of the tracks is plotted with a circle over the first point, and a triangle with the parcel's altitude at the last. These diagrams are interpreted schematically in terms of regions of flow with some of the boundaries identified as fronts. Figure 1 shows a pair of such diagrams at the mature stage to illustrate the labelling. An arrow which thickens towards its head indicates ascent in these diagrams. Region A denotes the flow of cold air round the north side of the system. Regions B and C contain warm air which rises at the warm front. Region B denotes such air when it turns left relative to the system and region C is that which turns to the right. Region D is the flow under the warm front towards the centre which ascends slowly.

3. DEVELOPMENT OF A BAROCLINIC WAVE

a. Initial Conditions and Summary

A broad jet was specified as the unperturbed state and a small wavenumber 6 perturbation superimposed on it. Figure 2 shows the vertical and meridional structure of the jet. It has a maximum speed of nearly 39 ms^{-1} at 45°N and 200 mb. The geopotential field was obtained from the perturbed motion field by solution of a reverse balance equation. At 1000 mb the perturbation amplitude in the geopotential field was 17 m. For the moist run, the moisture variable was set to 90% relative humidity at all grid points and levels up to 350 mb.

The structure of the developing depression is analysed at three stages which are summarised in Fig. 3. The first, at three days, is termed the linear stage since the features analysed can be described in terms of the linear theory of baroclinic instability. The low level velocities are slower than the motion of the wave and so the relative flow is from right to left. There is little vertical motion. The mature stage is analysed at 5 days and shows separate regions of flow separated by fronts. At both levels there is now a flow of air faster than the system on its south side. Finally, at 6 days an analysis is made of the occluding stage. Here, the regions of flow are becoming more complex as air circulates round the centre of the depression.

The effects of moisture are summarised in Fig. 4 which shows the extrema of the 1000 mb height field plotted at daily intervals. Differences are small in the first three days since a small amount of ascent is required to saturate the air. The height of the high pressure centre is little affected throughout the integration. However, the low pressure centre deepens much more rapidly in the moist case after day 3. Between days 4 and 5 it deepens at nearly twice the rate of the moist run and is about 10 mb deeper at day 5. However the rate of deepening decreases after this so that the two runs have similar values by day 7.

b. Linear Stage

The early stages of development will be summarised by looking at the 72 hour diagnostic fields and trajectories for the period 48-96 hours. Figure 5a shows the 1000 mb height field. The range of values is 74 m corresponding to about 10 mb pressure difference at the surface. At 500 mb (Fig. 5b) a pronounced trough had formed with its axis near 25°W , some 15° west of the surface centre. The amplitude of the

disturbance is 60 m at 50°N near the centre of the jet. The 1000 mb vorticity pattern is shown in Fig. 5. An arrowhead shaped pattern is evident with a maximum of $1.4 \times 10^{-5} \text{s}^{-1}$ near the surface pressure centre and arms of positive vorticity extending northwest and southwest from it. The 550 mb vertical velocity pattern (Fig. 5d) shows very small values (maximum ascent $0.4 \mu\text{b s}^{-1}$) everywhere. Ascent is greatest near 50°N 5°W , about 5° east of the surface centre, with regions of ascent extending to the northwest and south-southwest.

The diagnostic fields for the moist and dry runs are almost identical at this stage. However, the 550 mb vertical velocity reaches $0.7 \mu\text{b s}^{-1}$ in the moist run.

A set of trajectories was initiated at 48 hours on a grid covering the region around the low pressure centre. Figure 6 shows the tracks of parcels initially at 950 mb. In the dry run, Fig. 6a the almost constant size of the crosses indicates that little vertical motion is occurring. The parcels near the top left of the diagram show little evidence of the disturbance. Nearer the bottom of the diagram, parcels entering from the right deviate northwards with slight ascent while parcels being left behind by the system turn southwards and descend a little. These features are summarised in the schematic Fig. 6b. Figure 6c shows the same set of parcels for the moist run. The meridional and vertical displacements are generally much larger but the pattern of motion is the same.

At 750 mb (Fig. 7) an almost circular pattern is found since the system speed is close to the mean wind speed at this level. In both dry and moist runs there is clear evidence of ascent ahead of the centre and descent behind it. Rising parcels ascend up to 50 mb in

the dry run and 100 mb in the moist run. There is no evidence in either run for the formation of the flow discontinuities found at later stages of development.

c. Mature Stage

The mature stage of development is the time when the central pressure deepens most rapidly and the main non-linear features of the flow appear. It is also the time when the moist run shows the largest differences from the dry run. The period around 120 hours is analysed to represent this stage.

Figure 8a shows the 1000 mb height field. The low centre has moved northeastwards giving a pronounced asymmetry between the low and high pressure centres. The height range is now 238 m (about 32 mb in surface pressure) and the low has deepened 66 m in the preceding 24 hours. A pronounced trough can be traced south from the low centre to cross 0° longitude at about 43° N. There is also a slight indication at 49° N 18° E of a trough extending southeast from the centre. The 500 mb height field is shown in Fig. 8b. The trough axis is at about 5° W, 10° west of the surface centre, and shows some asymmetry due to the effects of the non-linear advection terms in the equations of motion. The 1000 mb relative vorticity field (Fig. 8c) has its maximum of cyclonic vorticity at 53° N 9° E on the eastern side of the surface pressure centre, and has an east-west orientation. From its eastern end, a secondary maximum extends southwestwards, parallel to the pressure trough and slightly ahead of it. The eastern end of the vorticity maximum is also the location of maximum ascent at 550 mb (Fig. 8d). The orientation of these features can be related to the low level temperature structure shown in Fig. 8e. Both pressure troughs lie on the 275 K isotherm. Note, however, that the tightest

part of the thermal gradient in the region east of the centre, is ahead of this between the 265 K and 270 K isotherms. Figure 8f shows the 500 mb vorticity field which has the arrowhead shape noted earlier at 1000 mb but with a larger region of cyclonic vorticity. The relationship of the main features presented above is displayed in Fig. 10. The region of maximum vorticity (solid line) is entirely within the region of ascent (dashed line). The region of tight thermal gradient to the southwest of the centre runs across from ascending to descending air and is behind the line of the secondary vorticity maximum. By contrast, the region of tight thermal gradient to the east of the centre lies within the regions of high vorticity and ascent with the maximum of each quantity close to the 275 K isotherm. The maximum ascent (L_W) is at the eastern end of the region of high vorticity and also the end of the tightest thermal gradient.

These results may be compared with day 5 of the integration described in § 4e of Hoskins and West (1979). Although their integration was performed using a channel model with cyclic boundary conditions, the structure of the basic jet and the scale of the perturbation are similar to those used here. In particular, the doubling period of their perturbation (1.3 days) is very close to that observed in the present results. Their Fig. 8 showed height and temperature fields at the lower boundary of the model at 5 days. It can be compared with the 1000 mb height field and 950 mb temperature field presented above but since these are not at the lower boundary of the model, exact comparison is not possible. The range of height is 250 m in Hoskins & West (1979) compared with 238 m in Fig. 8a. The shape of the temperature wave is also very similar. However, the maximum vorticity at this stage of their integration was nearly double the value of $5.9 \times 10^{-5} \text{ s}^{-1}$

shown in Fig. 8c (personal communication). This is almost certainly due to the implicit smoothing of the stretching term in the vorticity equation which is analysed in the Appendix. The high resolution permitted by the geostrophic coordinate transformation would make the effect of this negligible in Hoskins & West's results.

It has been remarked before that the mature stage shows the greatest differences between the dry and moist runs. Detailed differences may be analysed by comparing diagrams from Fig. 9 with their counterparts in Fig. 8. Figure 9a shows the 1000 mb height field with the low centre about 10 mb deeper than in Fig. 8a. The centre has a more elongated shape with the lowest pressure about 5° further east. Since the high pressure cell has not moved a considerable tightening of the gradient ahead of the depression has occurred. At 500 mb (Fig. 9b) the main trough has a similar amplitude and position. However, in the moist run, latent heat release has caused considerable distortion along the line of the surface warm front giving a deep trough in this region. The main difference in the 1000 mb vorticity field (Fig. 9c) is in the magnitude of the cyclonic maximum. For the moist run this is $13.6 \times 10^{-5} \text{ s}^{-1}$ in the eastern system compared to $5.9 \times 10^{-5} \text{ s}^{-1}$ in the dry run (Fig. 8c). A small cell of anticyclonic vorticity has also developed immediately south of the centre in a region of descending cold air. Figure 9d shows that this descent is balanced by locally enhanced ascent ahead of the cold front. The main region of ascent on the warm front has a vertical velocity over three times as great as in the dry run (Fig. 8d) while descent at its eastern end is twice as great. The distance between these two arms of the warm front circulation is 15° of longitude in Fig. 9d compared with 25° in Fig. 8d. This reduction in length scale has been achieved without

changing the scale of the whole system by splitting the vertical circulation into two. The second one is that noted above on the cold front. The 950 mb temperature fields (Figs 9e, 8e) are similar except that in the moist run, the cold air has advanced further south and east on the west side of the depression. This is indicated, for example, by the 270 K isotherm which has advanced 5° longitude eastwards at 50° N. The cold air has also advanced further southwards in the anticyclone (e.g. at 45° N 15° W). Finally, Fig. 9f shows the 500 mb relative vorticity field which shows the warm front trough clearly. Both cyclonic and anticyclonic vorticities have been enhanced in this region, the latter being three times as great at 50° N 30° W.

A grid of air parcel trajectories was initiated at 96 hours over a region covering the low pressure centre and was followed for 48 hours. Figure 11 shows a selection of tracks of parcels initially at 950 mb. At this stage the flow can be divided into distinct regions. Between them are two separation zones which parcels do not usually cross and which divide air coming from different origins. On this basis they are identified as fronts and marked with the usual symbols on the schematic. The separation zone marked by the cold front symbol divides regions A and B. That is, it separates cold air which has passed the northern side of the system and is now travelling southwestwards, from warm air which has been drawn into its southern side and is being accelerated towards the northeast. On the trajectory diagram Fig. 11a it shows up as a narrow region with air travelling in opposite directions on either side of it. The other separation zone is marked by the warm front symbol and is more difficult to see since the separation occurs in the vertical. However, the trajectories show that air approaching the southern side of this zone has taken a quite different course from the

relatively undisturbed westward flow on its northern side. When it reaches the front, the warm air approaching from the south ascends over the colder air and then turns sharply to the left to flow parallel to it but at a higher level. The deformation of fluid parcels during the motions depicted in Fig. 11 is well illustrated by Fig. 13. Here the parcel positions at 144 hours have been joined together in the rows and columns of the initial square grid at 96 hours, using the cross size to indicate altitude as before. The stretching out of parcels along the cold front is easily seen but the deformation occurring as parcels rise in the warm front region can also be discerned. It is interesting to note from this diagram the rapidity with which subsiding parcels behind the cold front have travelled round the southside of the anticyclone and are close to being absorbed in the next depression.

Two trajectories were marked in Fig. 11a for further study. Profiles of diagnostic quantities following each parcel are given in Fig. 14a, b. No 1 (Fig. 14a) is in region A and is a cold air parcel which starts northwest of the centre and travels southwards behind the cold front. Initially its track is horizontal but towards the end of the period it descends to 975 mb. Its relative vorticity starts at about $3 \times 10^{-5} \text{ s}^{-1}$ in the region of the cyclonic vorticity near the centre. This drops steadily due to compression of vortex lines in the divergent velocity field to end with about the same magnitude of anticyclonic vorticity. The increase in deformation towards the end of the period is due to the parcel approaching the cold front. Temperatures are not available below 950 mb since they are defined at mid-levels by the layer thickness and so cannot be plotted for this parcel. However, the initial temperature was -8°C . By contrast, the warm air parcel No 2 (Fig. 14b) starts with a temperature of $+5^{\circ}\text{C}$. It shows substantial

ascent reaching 829 mb by the end of the period. This parcel is in a convergent velocity field at all times and acquires substantial cyclonic vorticity by stretching. The abrupt change near 132 hours marks the parcel's sharp turn to the left and is indicated by an asterisk in Fig. 11a.

The general pattern of flow in the moist run (Fig. 12) is very similar to that shown in Fig. 11 for the dry run. The greater size of the crosses in regions of ascent indicates enhanced vertical motion while the greater length of the tracks shows that horizontal velocities are also greater. A feature of the pattern in Fig. 12 is the elongated shape of the centre which was also noted in the 1000 mb height field Fig. 9a. Ascending warm air parcels turn left at the warm front as in the dry run. However towards the end of the period the northern part of the cold front begins to change its structure as cold air parcels circulate round the south side of the centre. Details of individual trajectories in regions A and D are very similar to those in the dry run so a single example is given from region B in Fig. 14c (cf Fig. 14b). The greater horizontal speed of the moist parcel is indicated by its reaching the abrupt change marking the front at 122 hours instead of 132 hours. Soon after this it attains its maximum vertical velocity of $3.5 \mu\text{b s}^{-1}$ compared with $1 \mu\text{b s}^{-1}$ in Fig 14b. The overall ascent in the 48 hour period is 270 mb compared with 121 mb in the dry run.

At 750 mb, four regions of flow can be indentified although in the dry run only one of the boundaries separates the flow in such a way as to be labelled a front (Fig. 15). In particular, the boundary between regions A and B does not constitute a front at this level. It merely marks the trough line along which parcels stop descending. There is some evidence of a zone of confluence further east at which cold air

parcels from the west are juxtaposed with warmer air parcels from the east. However, the distinction is poorly marked. In contrast to this, the vertical separation at the warm front is much clearer here than at the lower level. There are two distinct streams of warm air travelling northwards and ascending over the lower air travelling west. The stream nearer to the centre turns left while the other turns right. The relationship of the final parcel positions to the 1000 mb height field is shown in Fig. 17. The distortion of the cells is much less than at 950 mb. However the deformation in the warm front region is shown very clearly. This diagram also confirms the lack of a front at this level to correspond to the surface cold front. Only weak deformation is indicated in this region.

Two parcels are marked in Fig. 15a for further study and profiles of diagnostic quantities following their motion are shown in Fig. 18a, b. No 1 is in region B (Fig. 18a) and shows marked ascent with a peak rate of ascent of $1.7 \mu\text{b s}^{-1}$ at 136 hours. The velocity field is slightly convergent at first, during which time the vorticity reaches $4 \times 10^{-5} \text{s}^{-1}$. The temperature drops steeply as the parcel ascends, keeping close to the dry adiabat. Calculated values of the temperature fall due to adiabatic ascent are marked on the diagram and verify the conservation of potential temperature by this parcel. The other parcel (Fig. 18b) also shows marked ascent reaching 567 mb. Its peak rate of ascent is reached in the middle of the period and is reduced nearly to zero by the end. At the same time the velocity field becomes weakly divergent and the very small vorticity becomes anticyclonic. These changes are associated with the parcel turning to the right during its ascent at the warm front.

The differences between the moist and dry runs at this level are similar to those at 950 mb. Figure 16 shows greater horizontal and vertical motion and a more elongated shape to the circulation than Fig. 15. However there is also a clear difference in Fig. 16 between the cold descending air and the warm ascending air in the cold front region south of the centre. This zone is therefore marked as a cold front in the schematic despite the horizontal velocities being the same on either side along much of its length. At the warm front most of the ascending parcels turn to the right with those nearest the centre showing the greatest altitude. On the south side of the centre, descending parcels travel round the centre and are marked in the schematic by region E. Figures 18c, d shows details of the two parcels corresponding to those in Fig. 18a, b in the dry run. Both show considerably enhanced vertical motion. Parcel No 1 (Fig. 18c of Fig. 18a) rises 250 mb at a peak rate of $4 \mu\text{b s}^{-1}$ in the moist run, compared with 183 mb at a peak of about $1.7 \mu\text{b s}^{-1}$ in the dry run. Parcel No 2 (Fig. 18d of Fig. 18b) rises 320 mb at a peak rate of $4 \mu\text{b s}^{-1}$ compared with 183 mb at a peak rate of $1.5 \mu\text{b s}^{-1}$. In both runs, the vertical velocity of the second parcel decreases towards the end as it turns right over the warm front. However, it reaches zero by 132 hours in the moist run and then starts to descend. The vorticity also becomes anticyclonic much earlier in the moist run. The calculated temperatures for dry and saturated adiabatic ascent have been added to Fig. 18d. The parcel closely follows the saturated values.

d. Occluding Stage

The final period of analysis is centred on 144 hours with trajectories computed for 48 hours from 120 hours. After 144 hours the low

pressure centre becomes stationary and the final stages of the non-linear development occur. Figure 19 is a composite diagram of the main diagnostic fields at this time. The overall height difference has increased to 303 m (about 52 mb surface pressure) with the low centre having a pressure of about 980 mb. The isotherms marked in Fig. 19 show that the region of warm air on the east side of the centre has formed a narrow tongue around the north side while cold air from the west has begun to form a tongue round the south side. The cold air incursion is marked by a region of anticyclonic vorticity and descent. The maximum cyclonic vorticity occurs at the surface pressure centre and has a value of about 10^{-4} s^{-1} . There is a secondary maximum along the cold front with values of about $3 \times 10^{-5} \text{ s}^{-1}$. The eastern end of the main vorticity maximum marks the region of greatest ascent at 550 mb. The largest value is $1.7 \mu \text{b s}^{-1}$.

These fields may be compared with Fig. 10 of Hoskins and West (1979). As in the mature stage, the height range agrees closely with their results. Their temperature pattern shows a rather less developed tongue of warm air round the north side of the centre and a sharper gradient at the cold front. The main differences are in the magnitudes of the relative vorticity maxima. Their diagram shows $3 \times 10^{-4} \text{ s}^{-1}$ at the pressure centre (cf 10^{-4} s^{-1} here) and $1.2 \times 10^{-4} \text{ s}^{-1}$ on the cold front (cf $0.3 \times 10^{-4} \text{ s}^{-1}$ here). The width of these regions of higher vorticity is, however, smaller than the grid length of the present model so it is inevitable that the integration scheme will smooth them out. The extent of the smoothing has been discussed earlier and in the Appendix.

The structure revealed by the low level diagnostic fields for the moist run at this stage is very similar to that shown above for the dry run except for the magnitudes. However, some interesting differences

have appeared at the top of the atmosphere by this time and these will be described here. Figures 20a, b compare the 350 mb vertical velocity fields for this time. The change in pattern between dry and moist runs is similar to that observed for the mature stage at 550 mb (Figs 8d, 9d). However, the biggest difference here is in the descent near 10°W which is twice as great in the moist run. The spacing between this and the warm front maximum of ascent is only 10° of longitude compared with 20° in the dry run. There is also a secondary circulation near the surface cold front at 48°W as was found in Fig. 9d. These differences are reflected in the 300 mb relative vorticity fields (Figs. 20c, d). As in Fig. 9c, there is considerable enhancement of cyclonic vorticity along the line of the surface warm front. However there is a much greater increase in the anticyclonic vorticity ahead of it. The pattern of enhanced vertical motion can also be seen in the thermal structure (Figs 20e, f). As would be expected at this level, the wave in Fig. 20e shows the warm air occupying more space than the cold air. In the moist run the warm air has generally advanced further north. However, the isotherms have also been distorted in the regions of large ascent and descent. At 35°W ascending air has created a warm area while at 15°W a cooler area has appeared in the region of descent.

Trajectory computations were performed in the same way as for the earlier stages. Figure 21 shows the dry run results for parcels initially at 950 mb. The schematic diagram shows a new region E where cold air from the north side of the system is circling round the south side instead of travelling down the cold front. The cold front is now more difficult to locate in this region since there is no difference in flow direction across it, although this characteristic still occurs at greater distances from the centre. However, a distinction can be drawn

between those parcels which originated to the right and are ascending, and those which came from the left and are descending slightly. The flow of warm air ahead of the cold front shows marked ascent (up to 160 mb in 48 hours) and the later parcels to reach the warm front show some reluctance to turn left, further emphasising the separation of flow there. At 750 mb (Fig. 22), the flow is similar to the mature stage (Fig. 15) except where the cold subsiding air has travelled round the south side of the centre. There is now a recognisable boundary between this air and the warm ascending air to the east and this has been marked as a cold front. Vertical motion is substantially greater than in Fig. 15 and a greater proportion of the warm air parcels turn right as they ascend over the warm front.

The moist run trajectories for this period are very similar to those presented in Figs 12, 16 for the mature stage. However a new feature does occur in the 950 mb pattern at this stage which is illustrated in Fig. 23. The southwesterly stream of air ahead of the surface cold front has become concentrated into a strong flow only two grid lengths across. Warm air feeds into it from the right, strengthening it. When this air flow reaches the warm front, it rises and turns right away from the centre. These features suggest that the model may be attempting to reproduce the low level jet described by Harrold (1973). The correct scale of jet is too narrow for the grid length of the model so it represents it by the narrowest feature it can i.e. two grid lengths across. It should be noted that this feature appears at a very late stage in the development of this system.

4. DISCUSSION

a. Dry run

The first stage of development was labelled the linear stage since the structure of the wave is largely that obtained by linear perturbation analysis. Eady (1949) performed the classical analysis by taking the quasi-geostrophic vorticity equation on an f plane and performing a normal mode perturbation analysis about a baroclinic mean state. The resulting eigenvalue problem yielded imaginary phase velocities (and hence instability) for waves longer than a defined minimum. The structure of an unstable wave can be found from the associated eigenfunction and a simplified composite diagram is shown in Fig. 24. The dominant characteristic is the westward tilt of the geopotential disturbance with height. The indications of temperature and vertical velocity apply only to the mid-level. The temperature phase lines slope eastward while those of the vertical velocity are almost vertical with a slight westward tilt. Subsequently, authors have investigated the effects of the earth's sphericity and of varying the mean wind profile (e.g. Green 1960, McIntyre 1970, Simmons & Hoskins 1976). The variation of Coriolis acceleration produced by the earth's sphericity was found to stabilise very long waves and to destabilise waves shorter than the limit found in Eady's analysis. However, the fastest growing wavelengths were little affected except by a small decrease in phase speed. The meridional structure of a basic state jet, such as that used in the present work, limits the meridional scale of disturbances which again stabilises very long waves. However, for unstable wavelengths it also causes a meridional dependence of the trough and ridge axes which leads to the arrow-head shape in the vorticity field noted in Fig. 5c. The

energy budget for a growing baroclinic wave can be obtained by suitable averaging of the momentum and thermodynamic equations (eg Holton 1979). For the eddy kinetic energy K' this yields

$$\frac{dK'}{dt} = \gamma \langle \omega' T' \rangle$$

where γ is a constant, the brackets indicate a zonal average and primed quantities are deviations from the zonal average. The equivalent equation for the eddy potential energy P' is

$$\frac{dP'}{dt} = \delta \langle v' T' \rangle - \gamma \langle \omega' T' \rangle$$

where δ is another constant. Thus eddy energy is gained by warm air ($T' > 0$) moving north ($v' > 0$) and cold air moving south ($T' < 0, v' < 0$), and becomes kinetic energy when warm air ascends ($T' > 0, \omega' > 0$) and cold air descends ($T' < 0, \omega' < 0$). In a baroclinic fluid these processes are accomplished by air parcel trajectories which lie between the isentropes and the geopotentials. This behaviour is well illustrated by Fig. 6 where parcels travelling through the system first perform a northward, upward excursion and then a southward, downward one. The constraints on this motion can be seen by analysing the ageostrophic flow (including the vertical motion) forced by the geostrophic motion. Hoskins et al (1978) have developed such a theory in a most elegant way enabling qualitative estimates of the forced circulations to be made in a rigorously based manner and providing a theoretical understanding of quantitative calculations. Their analysis yields an equation for the vertical velocity ($\frac{dz}{dt}$)

$$N^2 \nabla^2 \omega + f^2 \frac{\partial^2 \omega}{\partial z^2} = 2 \nabla \cdot \mathcal{Q}$$

where
$$\tilde{Q} = \left(-\frac{g}{\theta_0} \frac{\partial V_z}{\partial x} \cdot \nabla \theta, -\frac{g}{\theta_0} \frac{\partial V_z}{\partial y} \cdot \nabla \theta \right)$$

is a measure of the rate of change of horizontal potential temperature gradient on a fluid particle implied by the geostrophic motion. In order to retain thermal wind balance, the wind shear must change implying the creation of an ageostrophic velocity field. Under simplifying assumptions about vertical structure, they showed that cyclonically curved flow forces ascent ahead and descent behind the trough, and that confluent flow forces ascent on the warm side and descent on the cold side of the jet. Thus, as the thermal pattern around the wave is buckled, the pattern of development in Fig. 25 is generated with cyclonic development in the forward part of both regions of strong temperature gradient.

The formation of the fronts is a more complex problem although being related to the general development of the wave. Clearly, the ascent at the warm front and descent behind the cold front are related to the general forcing of vertical motion in these areas. Also, it has been seen that the cold front develops on the southwestward arm of cyclonic vorticity in the linear structure, while the warm front is an extension of the head of the arrowhead shape. Nevertheless, the flow shown in Fig. 6 does not contain fronts whereas that in Fig. 11 clearly does show them. Principal among the changes that have occurred between these diagrams is the reversal of relative flow on the south side of the centre. Two features of the system's development are associated with this. The first is that the pressure gradient near the centre has become strong enough to provide the acceleration needed to draw parcels inwards in this manner. The second is that the low level parcels spend an increasing amount of

time near the centre during which time they acquire large cyclonic vorticity due to the convergence in that region. After leaving it they travel comparatively rapidly along the cold front and so retain the vorticity until a considerable distance from the centre. The front therefore appears as a concentrated region of cyclonic vorticity. Clearly, this feature, and the warm air flow reversal with which it is associated can only appear below the steering level where the undisturbed flow is to the left. By contrast, parcels entering the warm front region have very little vorticity and acquire it directly as a result of the convergence there. Thus, the warm front appears as a relatively weak feature on the 1000 mb vorticity field until a late stage in the development. However, the trajectories indicate that a separation zone exists by the mature stage between the rising parcels coming from the south and the cold air stream from the east. This develops in the region of confluence seen at the linear stage on the northern side of the temperature gradient. The separation appears as a vertical one in which warm air parcels override cold air and then turn to travel parallel to them (Fig. 11). Near the steering level some of the rising air moves into increasing pressure gradients at higher levels and accelerates ahead of the system. This can be seen in region C of Fig. 15. The parcels in region B ascend into the upper trough which has weak gradients and so the parcels travel, as at lower levels, round the centre.

In the last stage of development, the warm and cold air streams have reached their greatest latitudinal displacements so the system ceases to gain energy. The trajectory diagrams show, however, that considerable vertical motion continues to convert eddy potential energy to eddy kinetic energy. The frontal zones extend further from

the centre in this period and become more alike at the two levels. The circulation of cold air round the south side of the centre removes the maximum ascent further from the centre and changes the character of the cold front. The trajectories indicate that relative flow is now parallel on the two sides of the front but with ascent on the east side and descent on the west side. The two streams of air are fed from opposite directions at their southern ends and the warm flow, in particular, is strengthened as it moves north-eastwards (Fig. 21).

b. Moist run

During the linear stage, the input of the latent heat energy causes an increase in growth rate without altering the baroclinic wave's structure. Increased vertical and horizontal motion was shown in Figs 6, 7. Growth continues at a greater rate in the later stages and the surface pressure reaches its lowest value about a day earlier than in the dry run. However, the presence of moisture also results in local changes to the structure, particularly near the warm front where latent heat release is concentrated. In Fig. 9 it was shown that this results in increased ascent associated with cyclonic vorticity generation and troughing of the height contours. This then leads to enhanced descent and anticyclonic vorticity generation downstream. The steep parcel trajectories in the warm front region imply a smaller scale of disturbance than the initial perturbation and this is confirmed by the spacing of the maxima of ascent and descent in Figs 9d, 20b. The scale of the primary vertical circulation in the baroclinic wave is determined in its early stages before saturation occurs. The extra heating due to condensation occurs in the region of ascent of the dry wave. This heating leads to a local enhancement of the thermal gradient and hence to an increased vertical wind shear through the thermal wind

equation. At the eastern end of the region of condensation, there is a diffluent region and enhanced forcing of descent. Thus a secondary circulation is forced on a smaller scale than the main wave. It consists of warm air rising at the warm front and acquiring cyclonic vorticity at low levels, then losing its vertical velocity as it approaches the tropopause and consequently acquiring anticyclonic vorticity. It then flows rapidly east parallel to the front, in an upper jet that has been strengthened in response to the increased thermal gradients below. Finally, it descends again in the high pressure region at the eastern end of the warm front.

Another secondary circulation appears on the cold front south of the centre. This can also be related to latent heat release in the ascending air on the warm side of the front. However, the descending arm of this circulation is immediately to the west giving an enhanced cross front circulation. The lower horizontal arm of this circulation helps to push the surface cold front forwards resulting in the cold air circulating round the centre at an early stage. Convergence associated with the ascending arm of this circulation contributes to the development of the narrow flow of air ahead of the cold front noted in Fig. 23. Thus the presence of moisture may assist the development of a cold front jet.

A few comments should be made on the realism of the experiment. Firstly, the effect of moisture is determined by the quantity present rather than the relative humidity. Since the 950 mb temperature in the warm air was only 2°C , the maximum moisture content was $4-5 \text{ gm kg}^{-1}$. Typical summer temperatures in western Europe would give values up to three times these. Secondly, there was no replenishment of moisture

through surface fluxes. Thus moisture was gradually lost from the model during the forecast. This will have particularly affected air which ascended again after descent to the surface.

5. CONCLUSIONS

The developing structure of an ideal baroclinic wave in a forecast model has been described using trajectory techniques. Three stages were analysed and a summary of the air flow at each stage was given in Fig. 3. At the linear stage there were no separation zones between different regions of flow. The trajectories were almost horizontal, and at low levels the air was left behind by the motion of the depression. At the mature stage, the warm air flow on the south side of the centre had accelerated to the system speed resulting in the formation of two flow discontinuities, a horizontal one at the cold front and a vertical one at the warm front. The final occluding stage showed cold air parcels circulating the pressure centre leading to a changed structure at the cold front. The flow patterns at the two levels became similar at this stage.

The mature and occluding stages were compared with equivalent times in an integration reported by Hoskins and West (1979) and qualitative agreement was found. The difference in magnitude of the cyclonic vorticity in frontal regions was explained in terms of numerical smoothing and the finer resolution available in their model through the use of the geostrophic coordinate transformation.

The main difference caused by the inclusion of moisture in the initial state was that the development proceeded more quickly and led to a more intense system with considerably greater horizontal and

vertical velocities. This was most noticeable at the mature stage when the rate of deepening of the low pressure centre was almost doubled. The local release of latent heat in ascending air resulted in the formation of secondary vertical circulations. In the warm front region a circulation was described with increased ascent in its western parts and descent at the eastern end. At the cold front, latent heat release was seen to enhance the cross front circulation and may assist the development of the cold front jet.

The analyses presented in section 3 describe the structural development of an ideal baroclinic wave and will serve as a basis for comparison with experiments using real initial conditions.

ACKNOWLEDGEMENTS

The work described in this paper was presented as part of a doctoral thesis of Reading University. I am grateful to my supervisors Prof. R P Pearce and Dr A J Gadd for their guidance and support throughout the course of the work. I am also grateful to Prof. B Hoskins, Mr A Gilchrist and Dr K Browning for discussion of the results. Staff of the Forecasting Research Branch of the Met Office provided the initial conditions for the integration. The diagrams were produced with the help of staff of the Data Processing and Central Forecasting Branches and were drawn by the Cartographic Section of the Met Office. I am grateful to the Met Office Typing Pool for preparing the manuscript.

Appendix: Derivation of a vorticity equation in finite differences for the Lax-Wendroff integration scheme.

The analysis is performed on the equation

$$\frac{\partial u}{\partial t} + u \frac{\partial u}{\partial x} + v \frac{\partial u}{\partial y} = 0 \quad (4)$$

The two step Lax-Wendroff integration scheme for Eq 4 may be written

$$u_{n+\frac{1}{2}} = \bar{u}_n^{xy} - \frac{\Delta t}{2} \left(\bar{u}_n^{xy} \delta_x \bar{u}_n^{xy} + \bar{v}_n^{xy} \delta_y \bar{u}_n^{xy} \right) \quad (5)$$

$$u_{n+1} = u_n - \Delta t \left(\bar{u}_{n+\frac{1}{2}}^{xy} \delta_x \bar{u}_{n+\frac{1}{2}}^{xy} + \bar{v}_{n+\frac{1}{2}}^{xy} \delta_y \bar{u}_{n+\frac{1}{2}}^{xy} \right) \quad (6)$$

where n is the time level and

$$\bar{u}^x \equiv (u(x, y) + u(x + \Delta x, y)) / 2$$

$$\delta_x u = (u(x + \Delta x, y) - u(x, y)) / \Delta x$$

and so on.

Note that $u_{n+\frac{1}{2}}$ is staggered by half a grid length in both directions from u_n and u_{n+1} .

Substituting Eq 5 into Eq 6 gives

$$\delta_t u = -u^{xy} \delta_x u^{xy} - v^{xy} \delta_y u^{xy} + O(\Delta t) \quad (7)$$

Similarly the v component of the momentum equation satisfies the relation

$$\delta_t v = - \overline{u}^{xy} \delta_x \overline{v}^{xy} - \overline{v}^{xy} \delta_y \overline{u}^{xy} + O(\Delta t) \quad (8)$$

In order to form the vorticity equation, Eqs 7, 8 are differentiated and subtracted with averaging applied where necessary. From the resulting expression the terms corresponding to the total derivative of vorticity may be extracted. The form of these terms is determined to maintain consistency with the advection terms in Eqs 7, 8. Thus

$$u \frac{\partial}{\partial x} \left(\frac{\partial \omega}{\partial y} \right) \equiv \overline{u}^{xy} \delta_x \delta_y \overline{\omega}^{xy} \quad (9)$$

The remaining terms are those associated with the stretching term of the vorticity equation and have the form

$$\mathcal{L} \mathcal{D} \equiv \overline{\delta_x v}^{xy} (\delta_x \overline{u}^{xy} + \delta_y \overline{v}^{xy}) - \overline{\delta_y u}^{xy} (\delta_x \overline{u}^{xy} + \delta_y \overline{v}^{xy}) \quad (10)$$

which is close to $\overline{\mathcal{L}_0 \mathcal{D}_0}^{xy}$ where \mathcal{L}_0 , \mathcal{D}_0 are the simplest finite difference forms of the vorticity and divergence on this grid.

This is equivalent to the application of a nine-point smoothing operator to each field separately. Trial calculations have shown reductions of over half in frontal regions when this smoothing operator was applied to either quantity.

REFERENCES

- Bjerknes, J 1918 On the structure of moving cyclones.
Geofys.Publik.Norske Videnskans - Akad. Oslo 1 No 2.
- Bjerknes, J and Solberg, H 1922 Life cycle of cyclones and the polar front theory of atmospheric circulation.
Geofys.Publik.Norske Videnskans - Akad. Oslo 3 No.1 pp 1-18.
- Browning, K A and Harrold, T W 1969 Air motion and precipitation growth in a wave depression.
Quart.J.Roy.Met S,95 pp 288-309.
- Burridge, D M and Gadd, A J 1977 The Meteorological Office operational 10-level numerical weather prediction model (December 1975). Sci.Pap. Met O No.34 HMSO London.
- Charney, J G 1947 The dynamics of long waves in a baroclinic westerly current
J.Met 4 pp 135-163.
- Danielson, E F 1961 Trajectories: Isobaric, Isentropic and Actual.
J.Met.18 pp 479-486.
- Djuric, D 1961 On the accuracy of air trajectory computations.
J.Met.18 pp 597-605.

- Eady, E.T. 1949 Long waves and Cyclone waves.
Tellus 1 pp 33-52.
- Gadd, A.J. 1978a A split explicit integration
scheme for numerical weather
prediction.
Quart.J.Roy.Met.S. 104 pp 569-582.
- Gadd, A.J. 1978b A numerical advection scheme with
small phase errors.
Quart.J.Roy.Met.S. 104 pp 583-594.
- Gadd, A.J. 1980 Two refinements of the split
explicit integration scheme.
Quart.J.Roy.Met.S 106 pp 215-220.
- Gilchrist, A. 1971 An example of synoptic development
in a general circulation model.
Quart.J.Roy.Met.S 97 pp 340-347.
- Golding, B.W. 1981 Diagnostic studies of mid-latitude
depressions.
Ph.D thesis University of Reading.
- Green, J.S.A. 1960 A problem in baroclinic stability.
Quart.J.Roy.Met.S.86 pp 237-251.
- Green, J.S.A. Ludlam, F.H.
and McIlveen, J.F.R. 1966 Isentropic relative-flow analysis
and the parcel theory.
Quart.J.Roy.Met.S.92 pp 210-219.
- Holton, J.R. 1979 An introduction to dynamic
meteorology.
Int.Geoph.Ser.Vol.23,
Academic Press, New York.

- Hoskins, B.J. 1975 The geostrophic momentum approximation and the semi-geostrophic equations. J.Atmos.Sci.32 pp 233-242.
- Hoskins, B.J. and Bretherton, F.P. 1972 Atmospheric frontogenesis models: mathematical formulation and solution. J.Atmos.Sci.29 pp 11-37.
- Hoskins, B.J. and West, N.V. 1979 Baroclinic waves and frontogenesis. Part II Uniform potential vorticity jet flows - cold and warm fronts. J.Atmos.Sci.36 pp 1663-1680.
- Hoskins, B.J. Draghici, I and Davies, H.C. 1978 A new look at the ω - equation. Quart.J.Roy.Met.S. 104 pp 31-38.
- McIntyre, M.E. 1970 On the non-separable baroclinic parallel flow instability problem. J.Fluid Mech.40 pp 273-306.
- Mudrick, S.E. 1974 A numerical study of frontogenesis. J.Atmos.Sci.31 pp 869-892.
- Pedlosky, J. 1970 Finite amplitude baroclinic waves. J.Atmos.Sci.27 pp 15-30.
- Simmons, A.J. and Hoskins, B.J. 1976 Baroclinic instability on the sphere: normal modes of the primitive and quasi-geostrophic equations. J.Atmos.Sci.33 pp 1454-1477.

LIST OF FIGURES

- Fig. 1 Idealised schematics of a mature depression at a) 950 mb
b) 750 mb.
- Fig. 2 Profiles of the basic state jet. a) Latitude cross
section at 200 mb. b) Vertical cross section near 45°N.
- Fig. 3 Summary of development of relative air flow in a baroclinic
wave.
- Fig. 4 Comparison of 1000 mb height extremes in the dry and moist
runs.
- Fig. 5 72 hour forecast fields - dry run
a) 1000 mb height in gpm. b) 500 mb height in gpm.
c) 1000 mb relative vorticity in $s^{-1} \times 10^5$. d) 550 mb
vertical velocity in $\mu b s^{-1}$.
- Fig. 6 diagnosed trajectories for 48-96 hours for parcels
initially at 950 mb. a) computed tracks - dry run.
b) schematic interpretation. c) computed tracks - moist
run.
- Fig. 7 Diagnosed trajectories for 48-96 hours for parcels
initially at 750 mb. a) computed tracks - dry run.
b) schematic interpretation. c) computed tracks - moist
run.
- Fig. 8 120 hour forecast fields - dry run
a) 1000 mb height in gpm. b) 500 mb height in gpm.
c) 1000 mb relative vorticity in $s^{-1} \times 10^5$. d) 550 mb
vertical velocity in $\mu b s^{-1}$. e) 950 mb temperature in K.
f) 500 mb relative vorticity in $s^{-1} \times 10^5$.

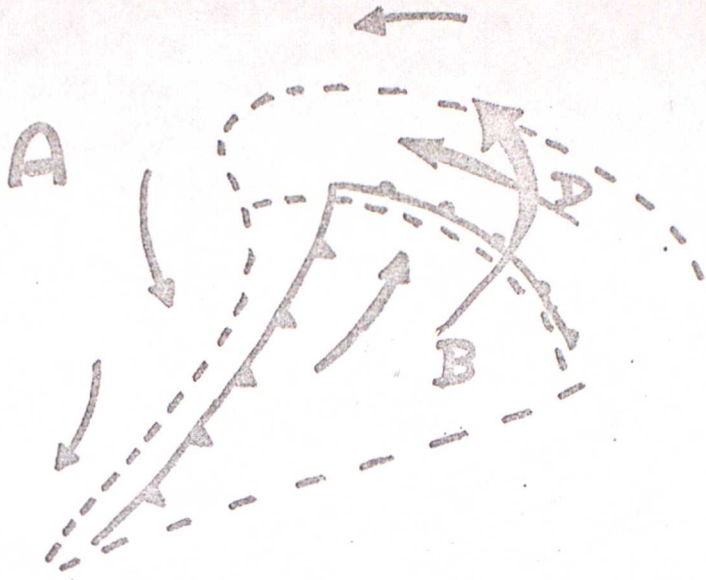
- Fig. 9 120 hour forecast fields -- moist run
a) 1000 mb height in gpm. b) 500 mb height in gpm.
c) 1000 mb relative vorticity in $s^{-1} \times 10^5$. d) 550 mb
vertical velocity in $\mu b s^{-1}$. e) 950 mb temperature in K.
f) 500 mb relative vorticity in $s^{-1} \times 10^5$.
- Fig. 10 120 hour composite diagram of the dry run forecast fields.
- Fig. 11 Diagnosed trajectories for 96-144 hours for parcels
initially at 950 mb -- dry run
a) selection of computed tracks. b) schematic inter-
pretation.
- Fig. 12 Diagnosed trajectories for 96-144 hours for parcels
initially at 950 mb -- moist run
a) selection of computed tracks. b) schematic inter-
pretation.
- Fig. 13 Final positions of the grid of air parcels initially at
950 mb superimposed on the 144 hour forecast of 1000 mb
height -- dry run
- Fig. 14 Profiles of diagnostic quantities following individual
parcels. a) Parcel No 1 in Fig. 11 (dry run).
b) Parcel No 2 in Fig. 11 (dry run). c) Parcel No 1 in
Fig. 12 (moist run)
- Fig. 15 Diagnosed trajectories for 96-144 hours for parcels
initially at 750 mb -- dry run
a) selection of computed tracks. b) schematic inter-
pretation.
- Fig. 16 Diagnosed trajectories for 96-144 hours for parcels
initially at 750 mb -- moist run

- a) selection of computed tracks. b) schematic interpretation.
- Fig. 17 Final positions of the grid of air parcels initially at 750 mb superimposed on the 144 hour forecast of 1000 mb height -- dry run.
- Fig. 18 Profiles of diagnostic quantities following individual parcels. a) Parcel No 1 in Fig. 15 (dry run). b) Parcel No 2 in Fig. 15 (dry run). c) Parcel No 1 in Fig. 16 (moist run). d) Parcel No 2 in Fig. 16 (moist run)
- Fig. 19 144 hour composite diagram of the dry run forecast fields.
- Fig. 20 144 hour forecast fields. 350 mb vertical velocity in $\mu\text{b s}^{-1}$ for a) dry run b) moist run. 300 mb relative vorticity in $\text{s}^{-1} \times 10^5$ for c) dry run d) moist run. 350 mb temperature in K for e) dry run f) moist run.
- Fig. 21 Diagnosed trajectories for 120-168 hours for parcels initially at 950 mb -- dry run
a) selection of computed tracks. b) schematic interpretation.
- Fig. 22 Diagnosed trajectories for 120-168 hours for parcels initially at 750 mb -- dry run
a) selection of computed tracks. b) schematic interpretation.
- Fig. 23 Diagnosed trajectories for 120-168 hours for parcels initially at 950 mb -- moist run.
a) selection of computed tracks. b) schematic interpretation.

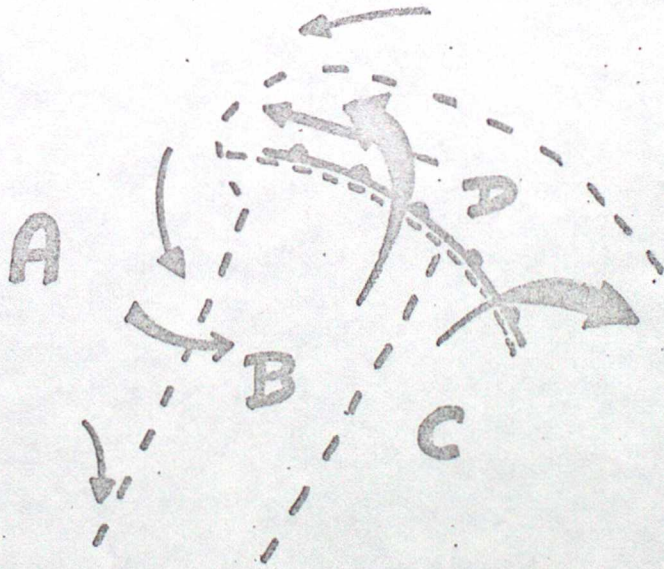
Fig. 24 Simplified structure of an unstable baroclinic wave showing phase relationships between the geopotential, temperature and vertical motion.

Fig. 25 Development areas predicted by simple application of Q-theory to the thermal structure of a developing depression.

a)



b)



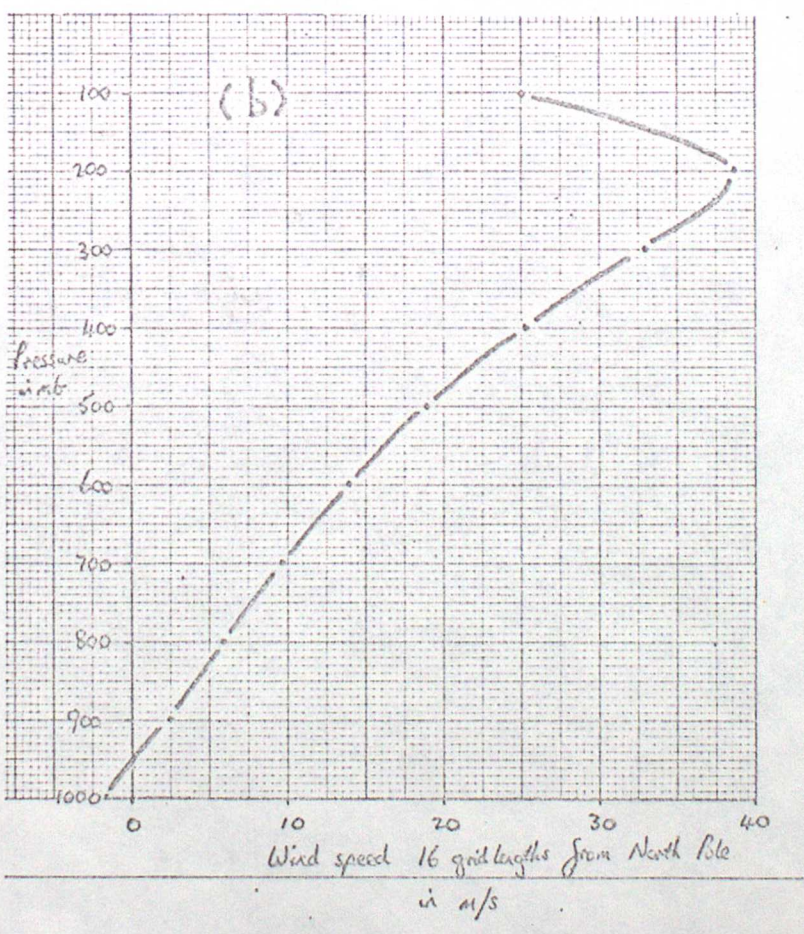
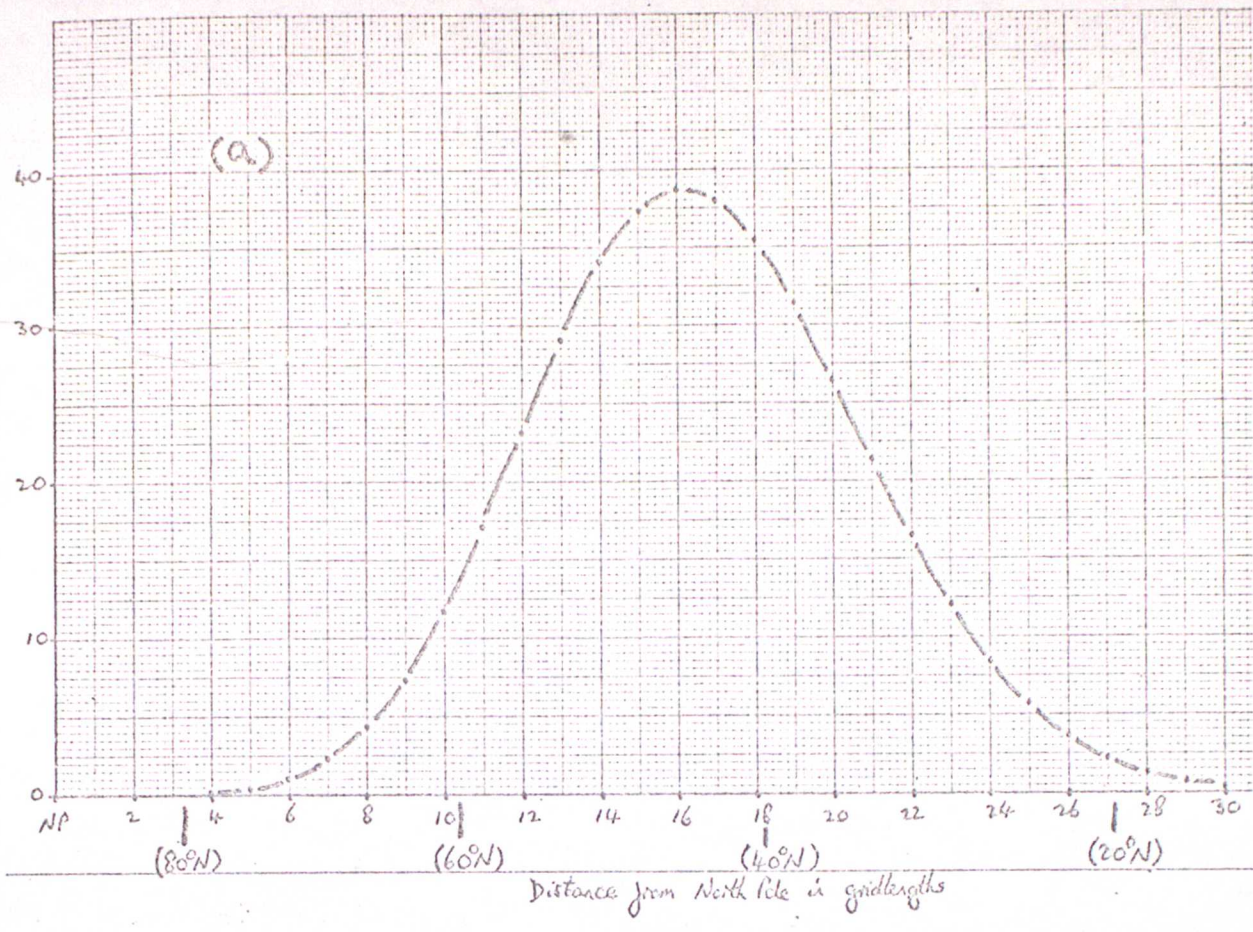


Fig 3

950mb

750mb

LINEAR

STAGE

DAYS 1-3



MATURE

STAGE

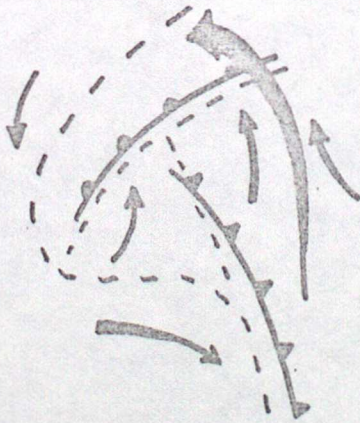
DAYS 4-5



OCCCLUDING

STAGE

DAYS 6-



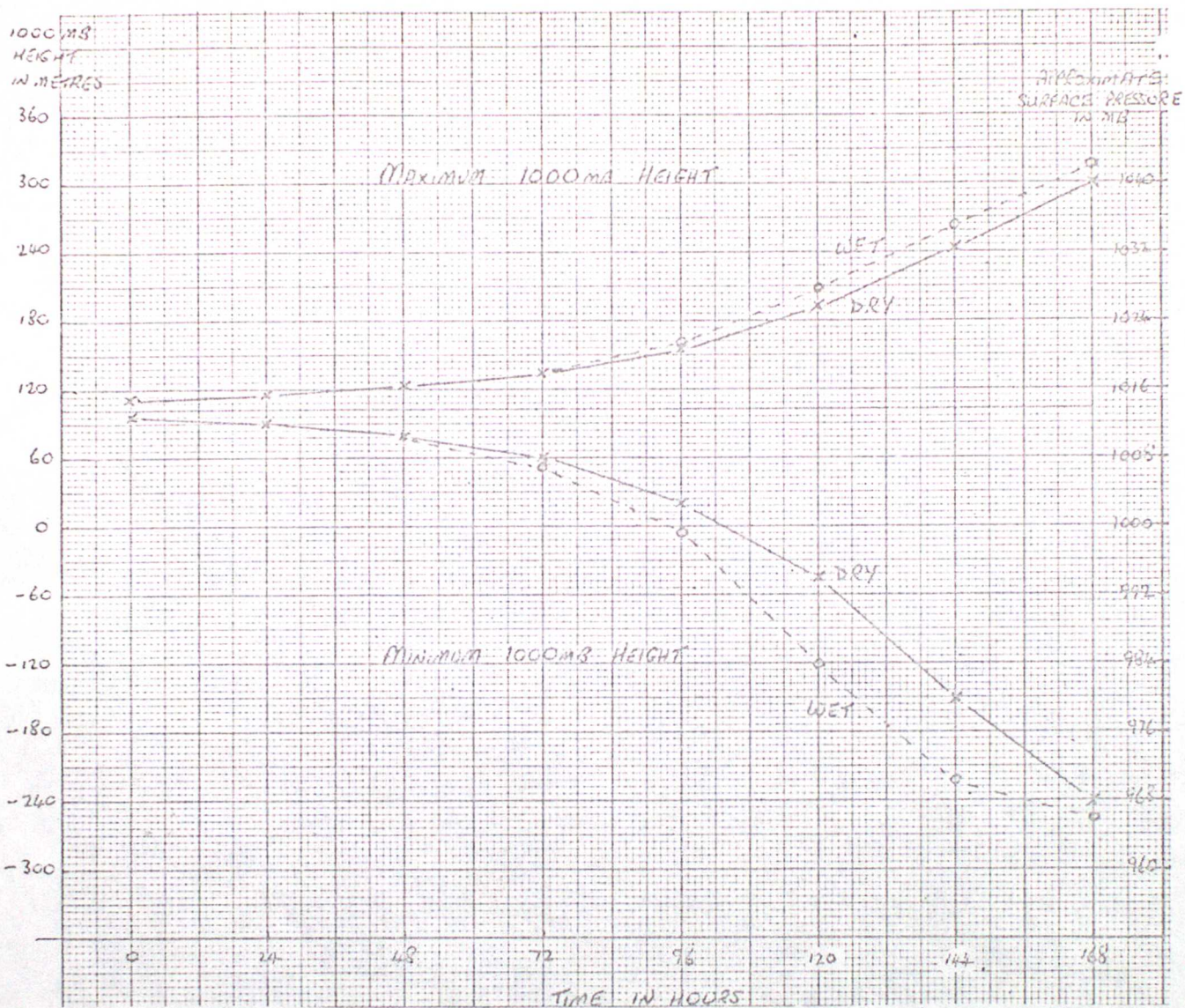


Fig 4



Fig 5a

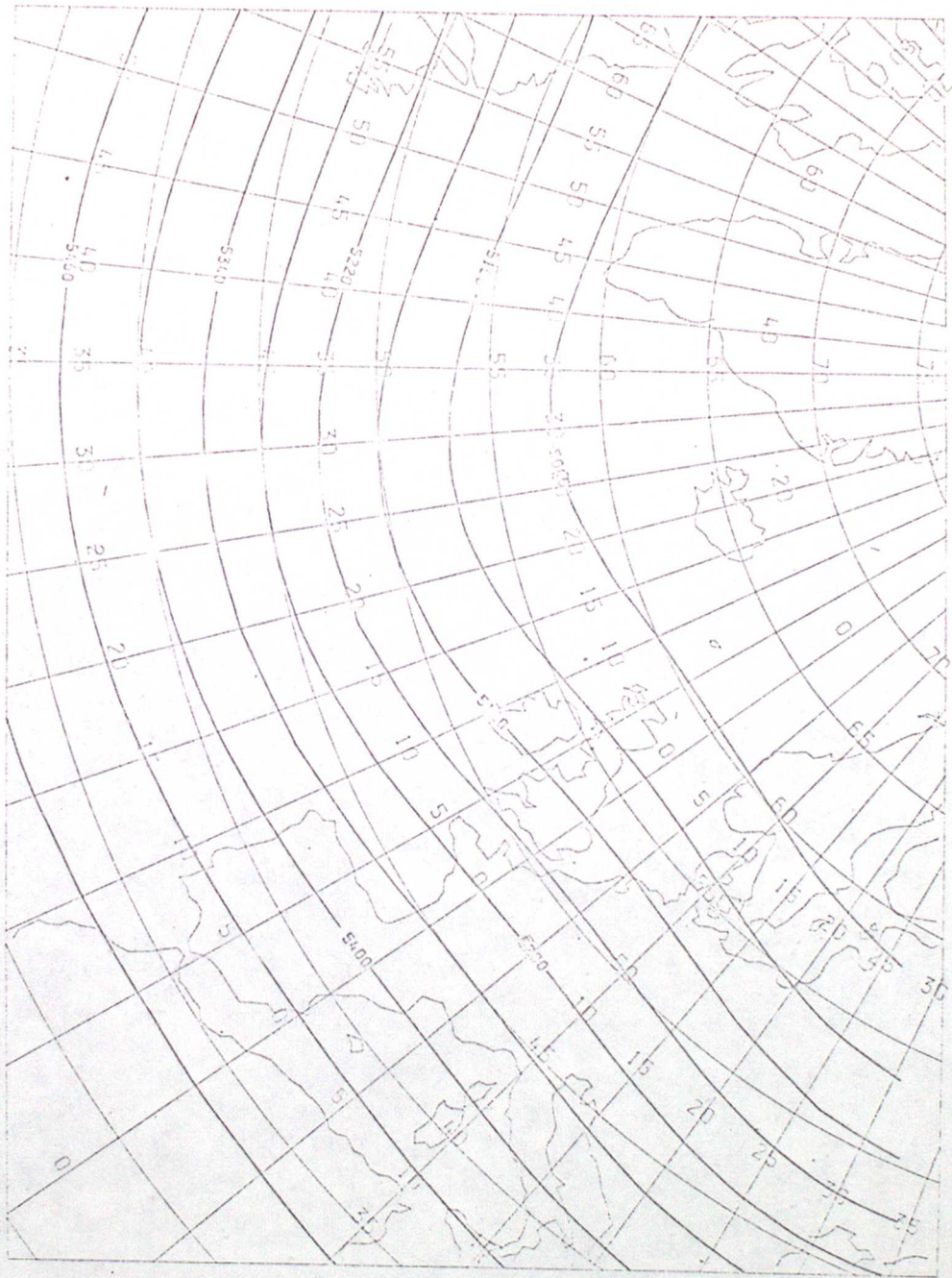


Fig 56

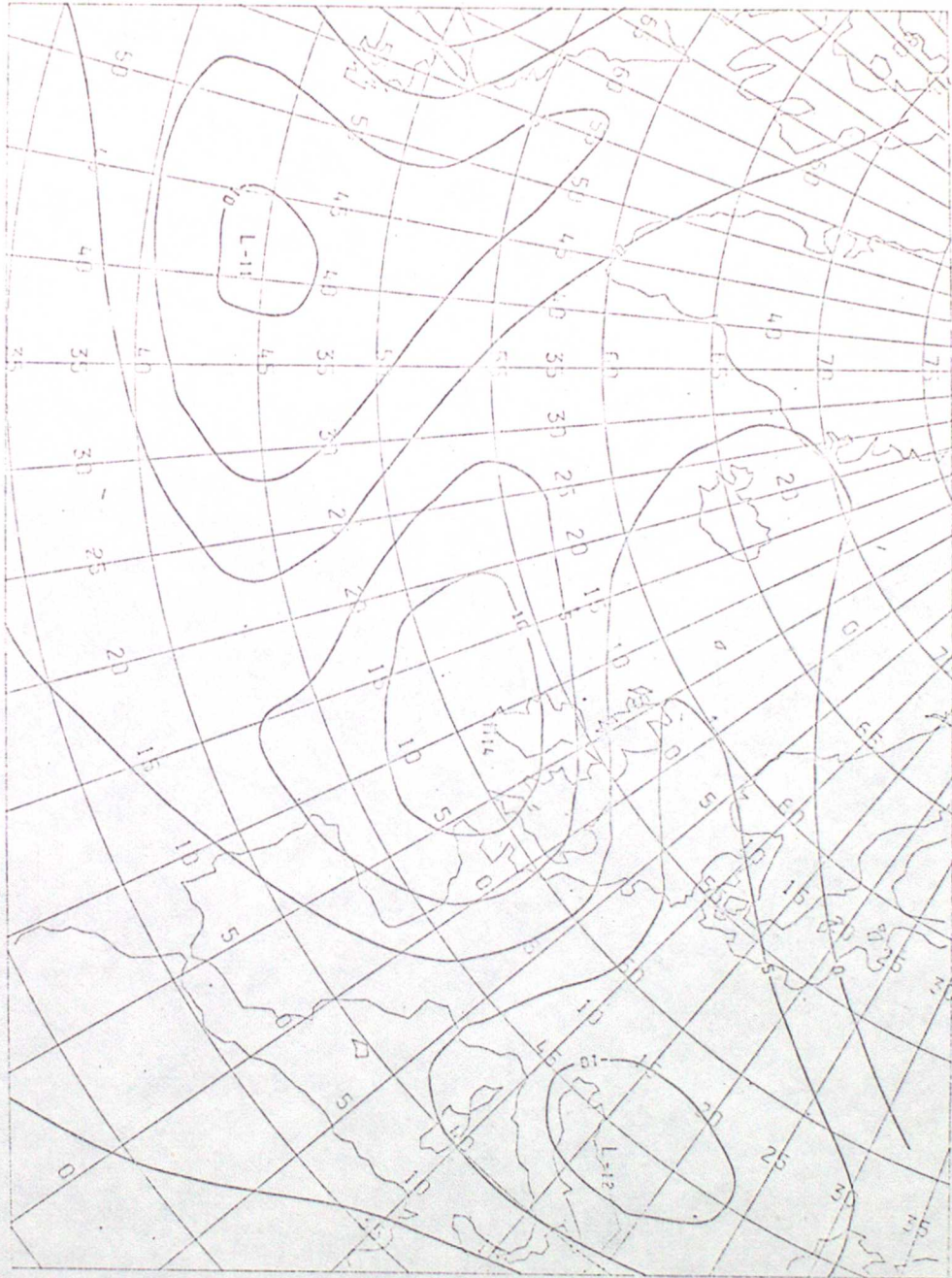


Fig 5c



Fig 5d

SIZE OF CROSS AT 950MB +

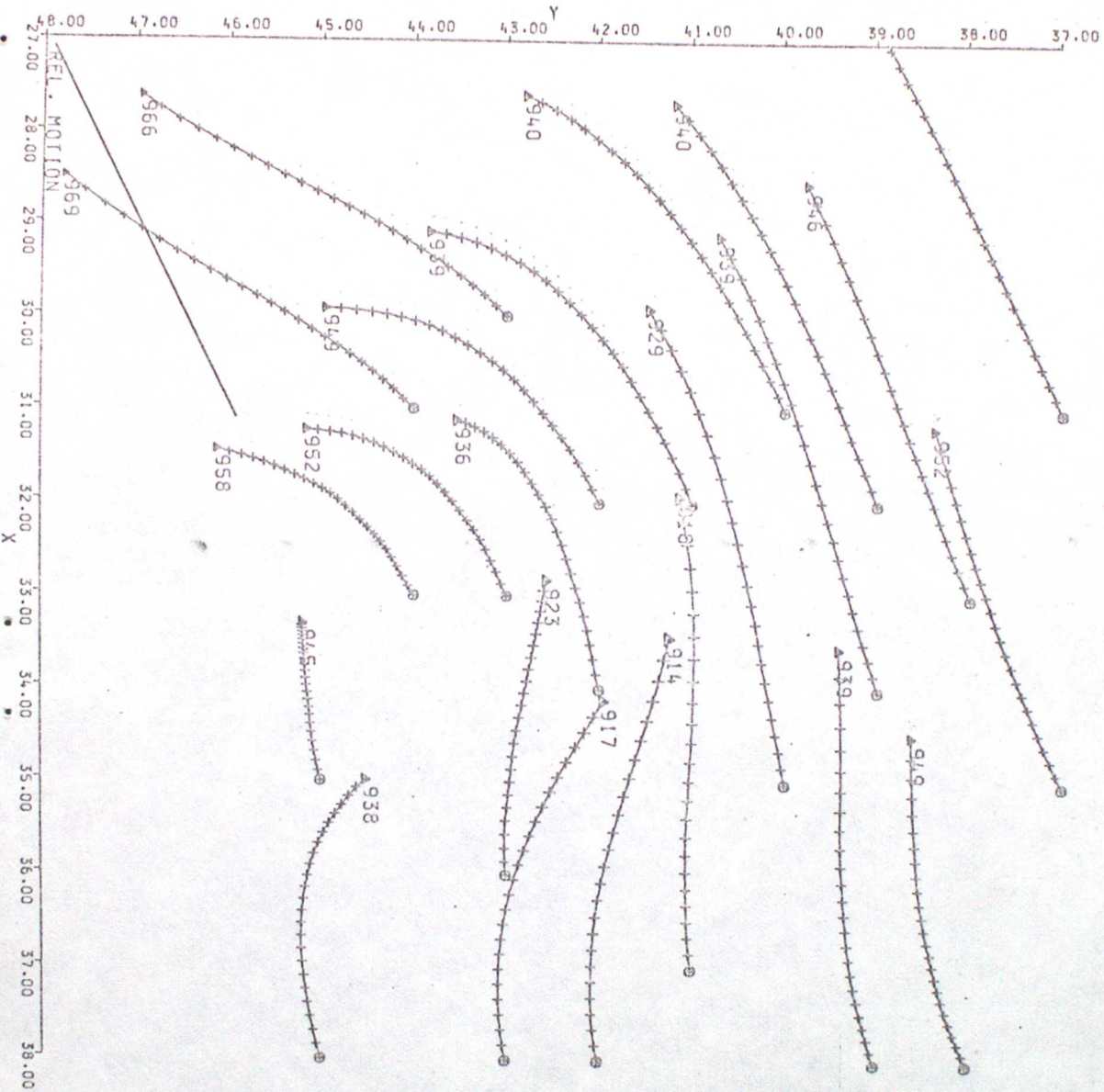


Fig 6a

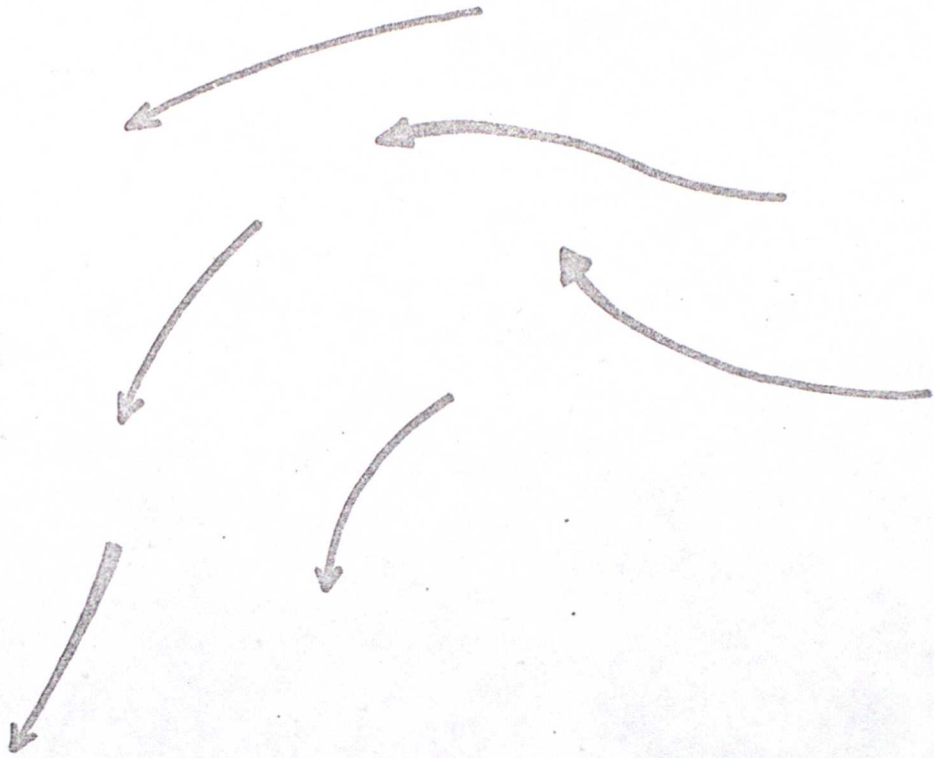


Fig 66

SIZE OF CROSS AT 950MB +

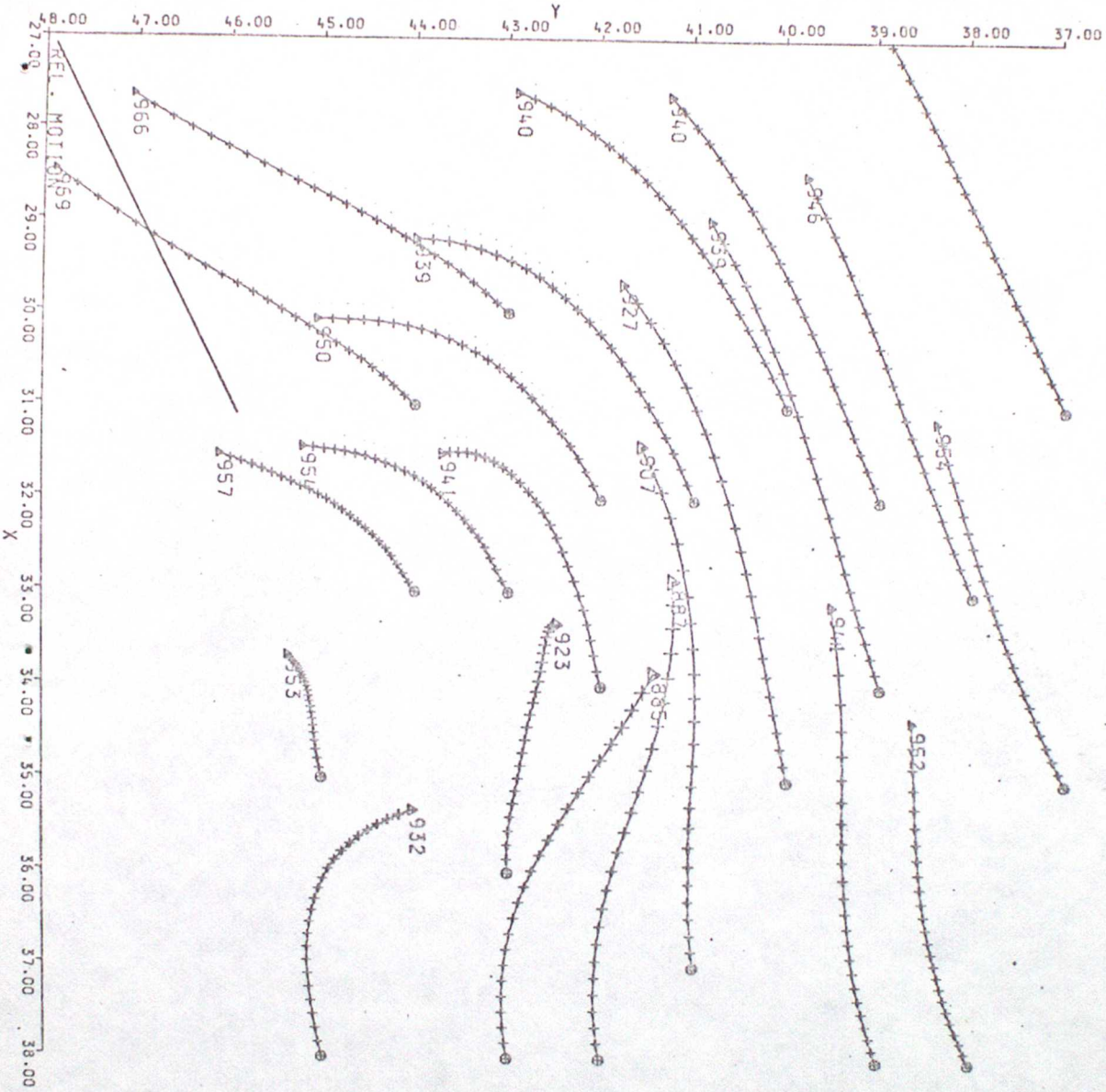


Fig 6c

SIZE OF CROSS AT 750MB +

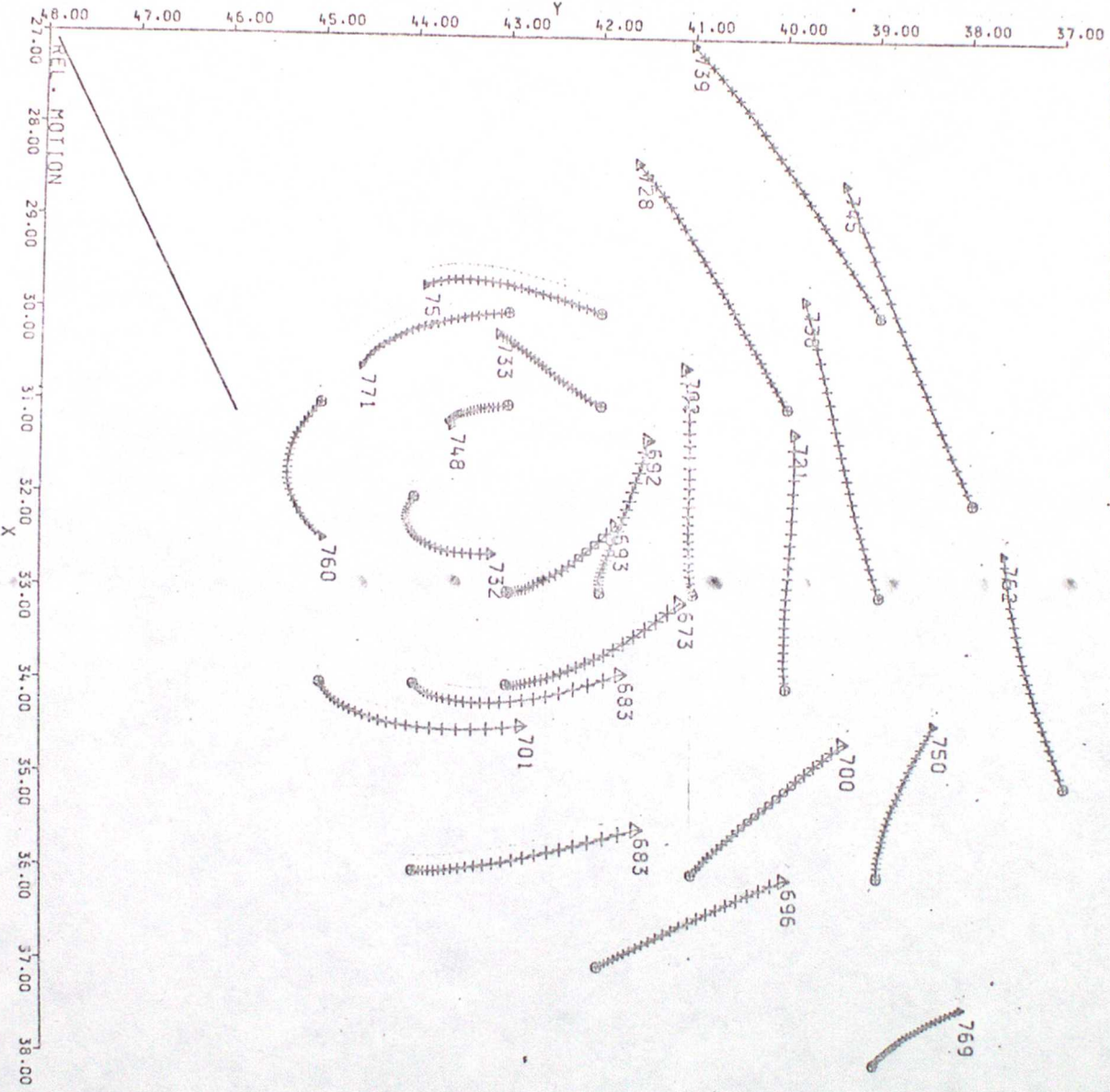


Fig 7a



Fig 76

SIZE OF CROSS AT 750MB +

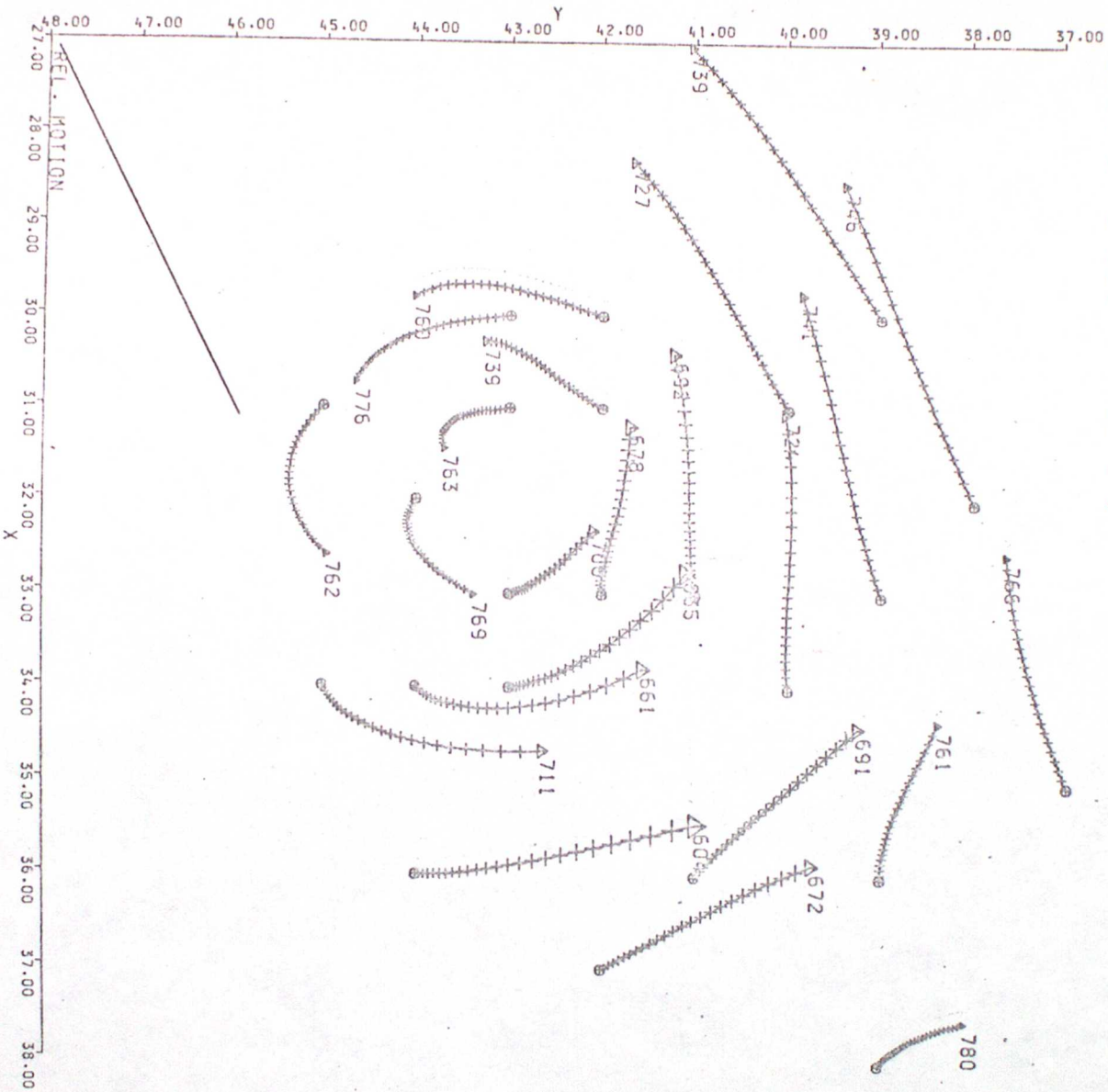


Fig 7c



Fig 8a

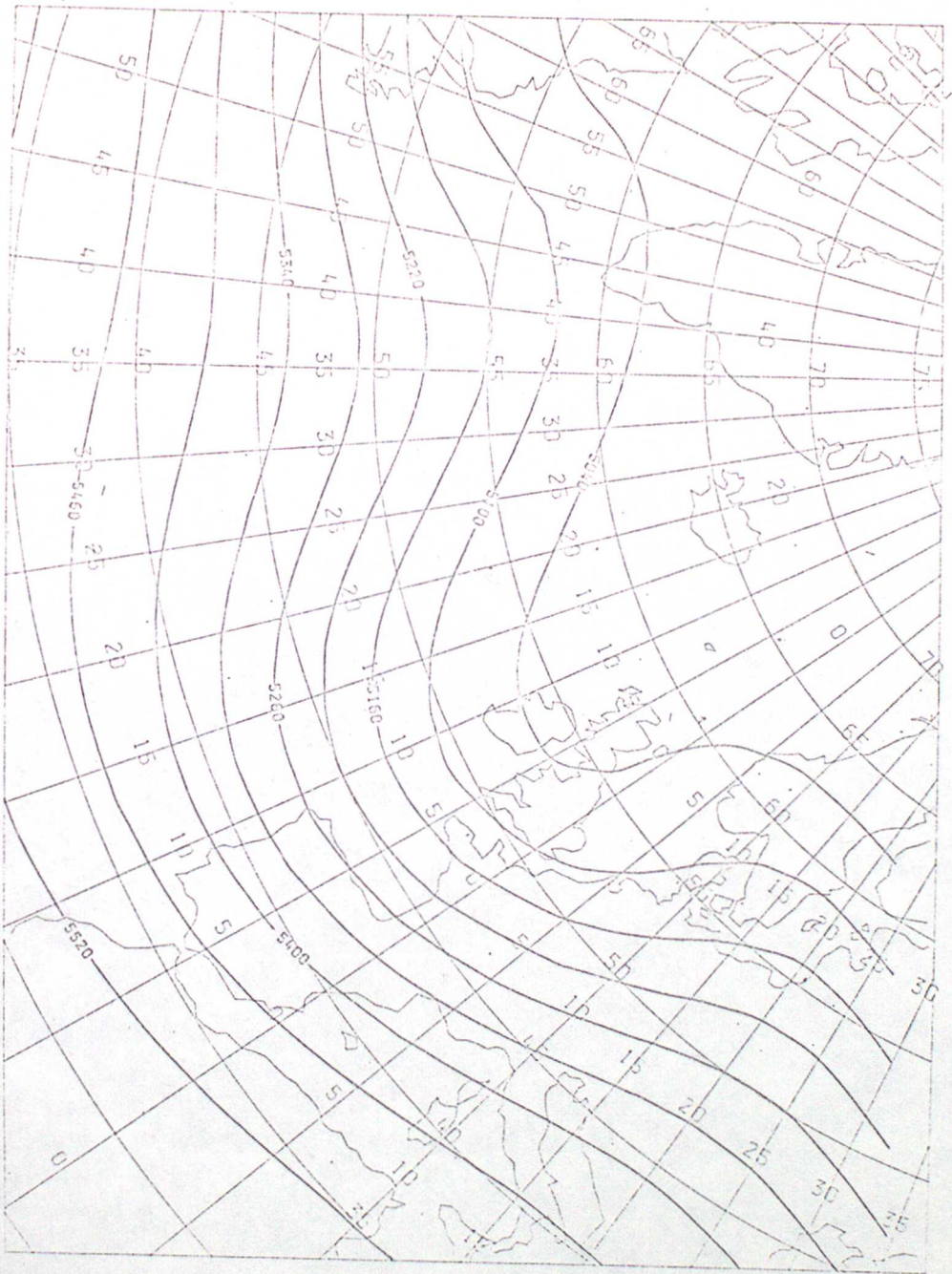


Fig 86

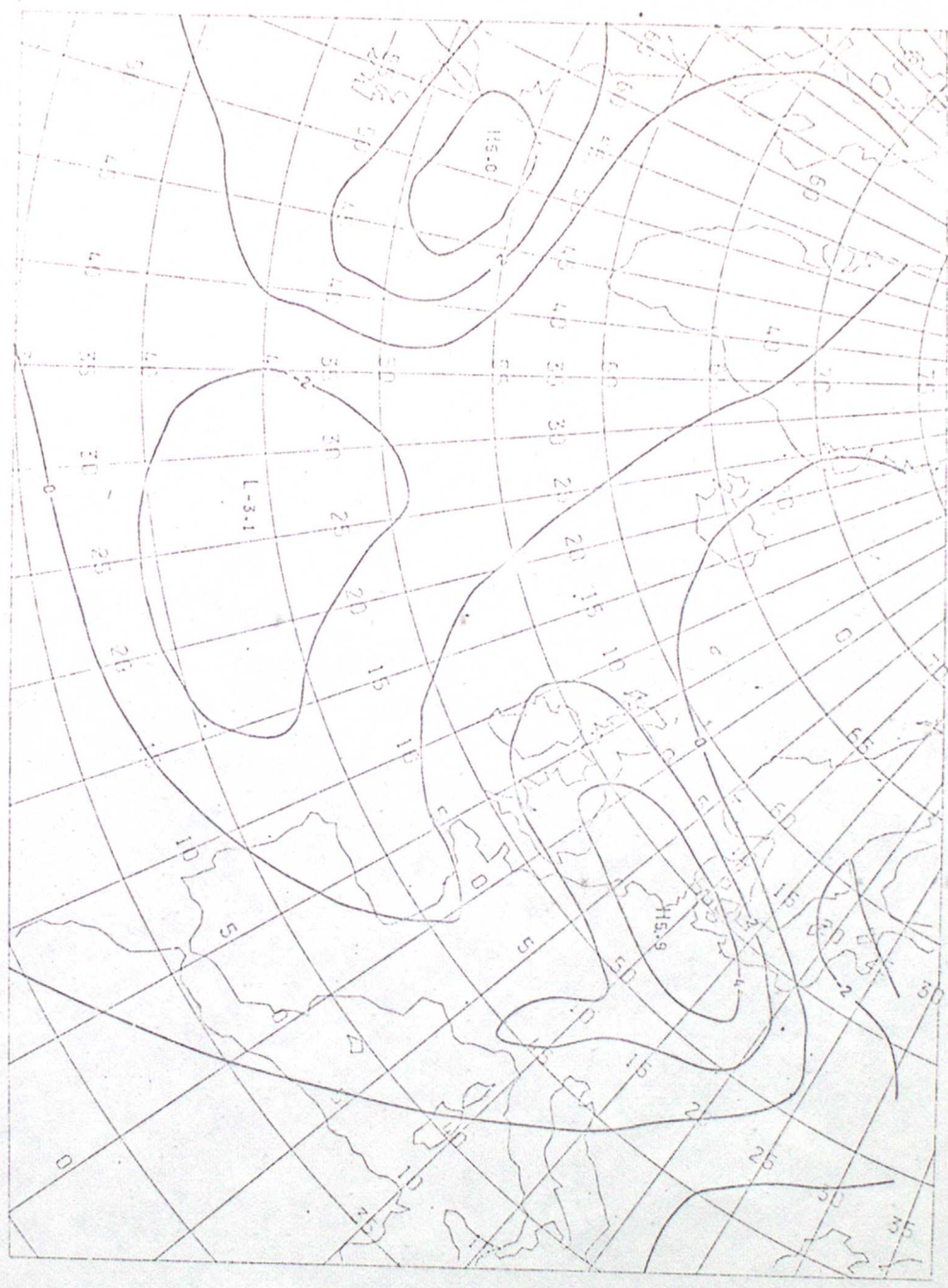


Fig 8c

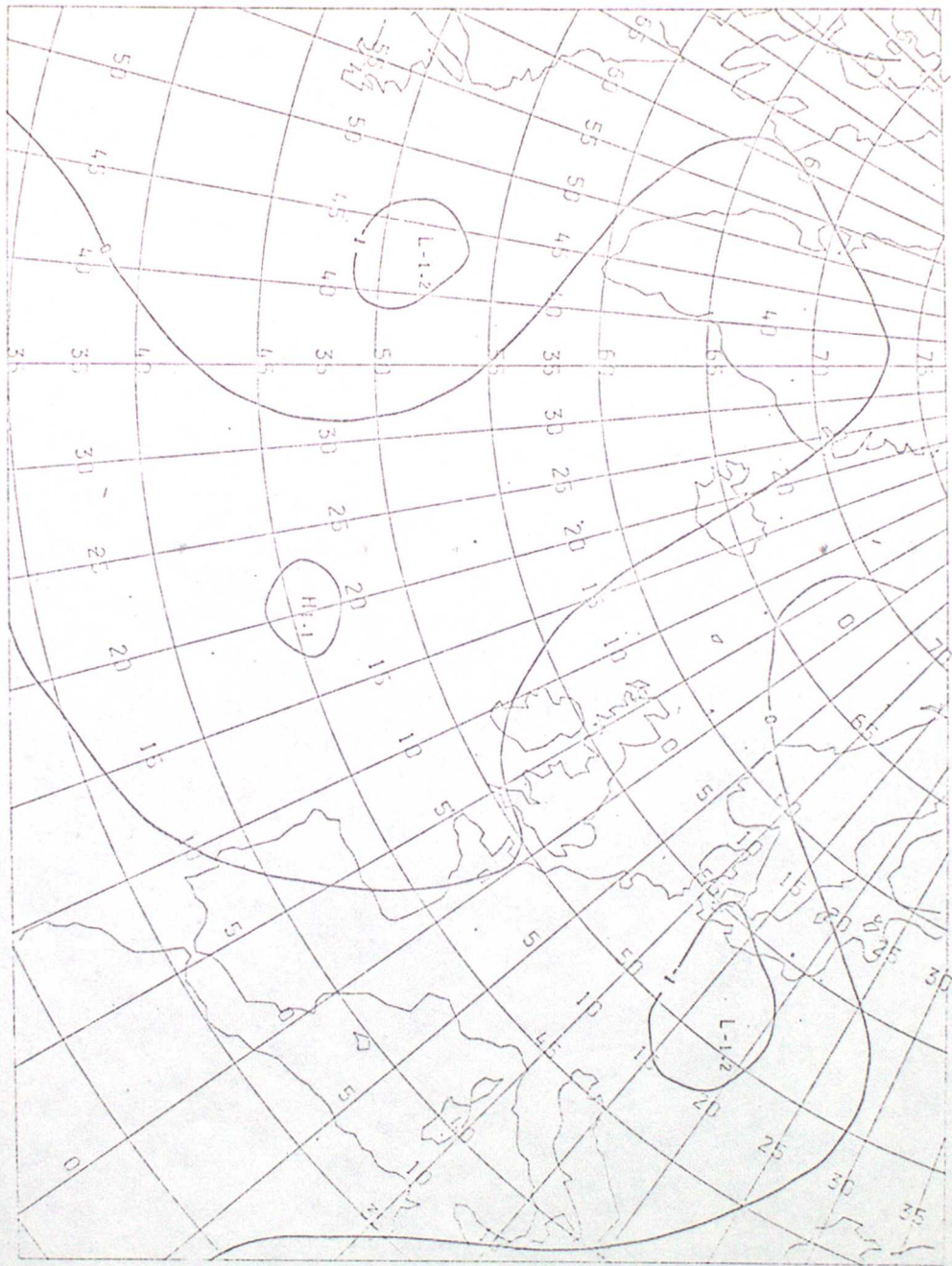


Fig 8d

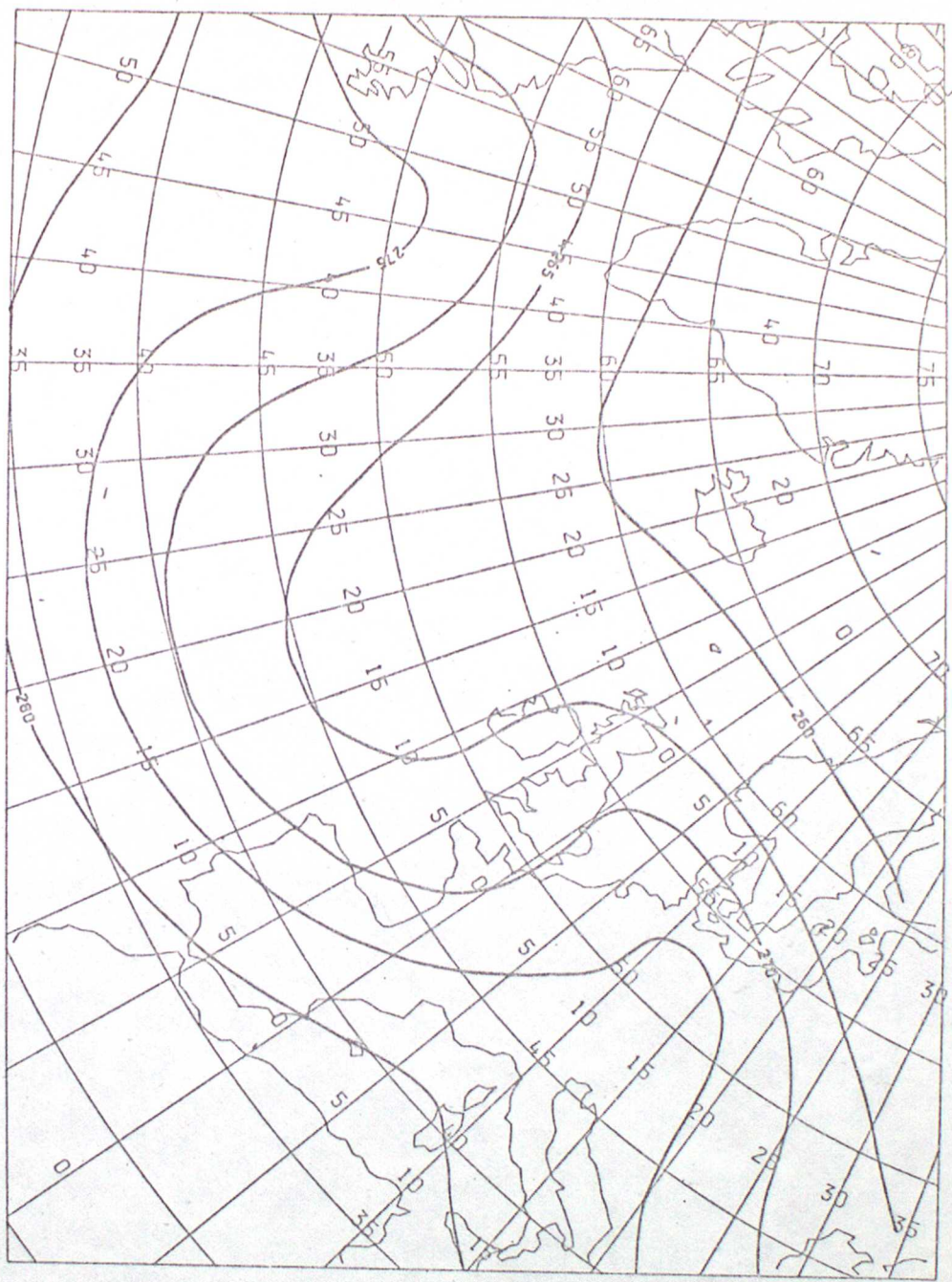


Fig 8e



Fig 8f



Fig 9a



Fig 96



Fig 9c

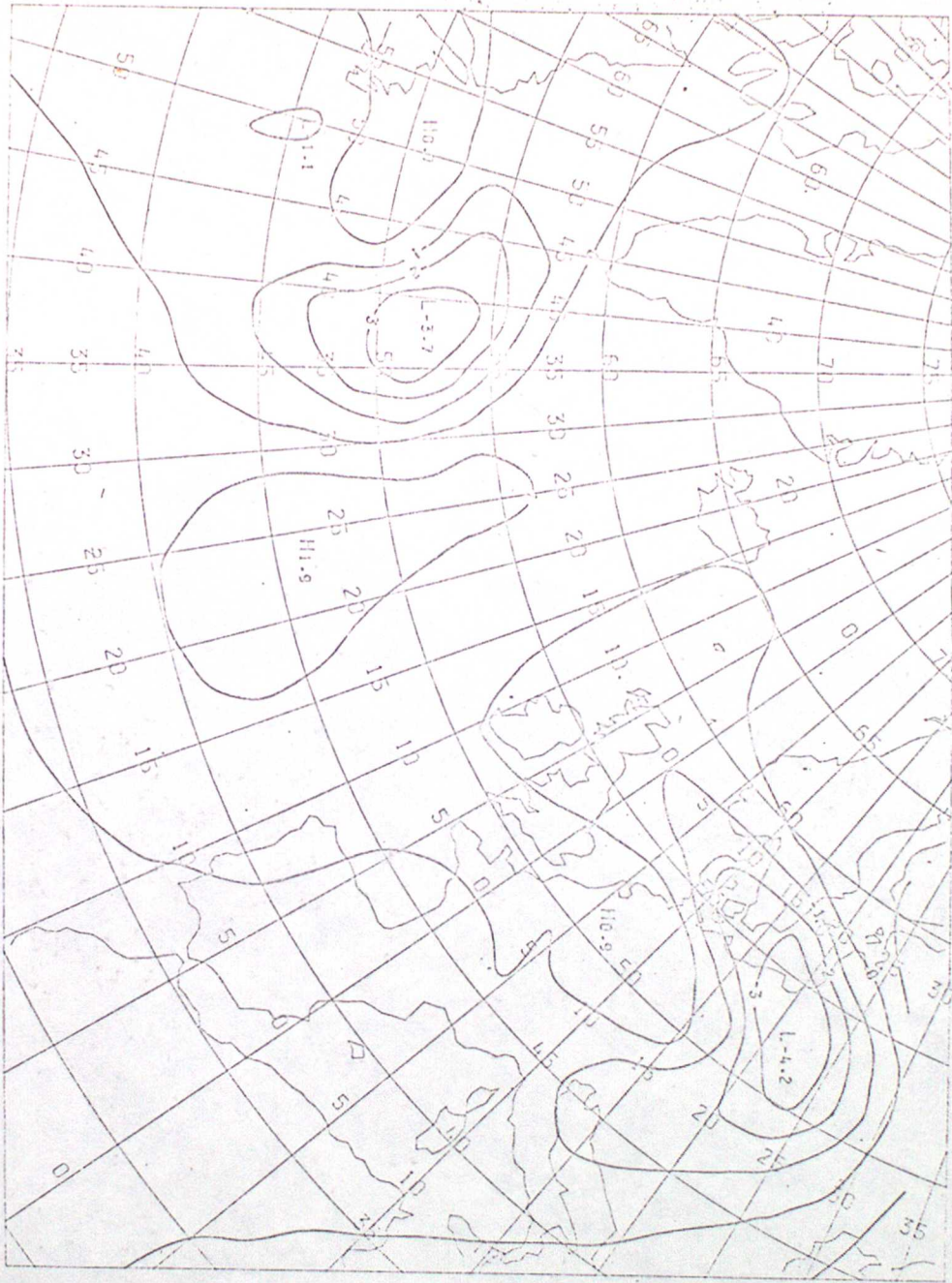


Fig 9d

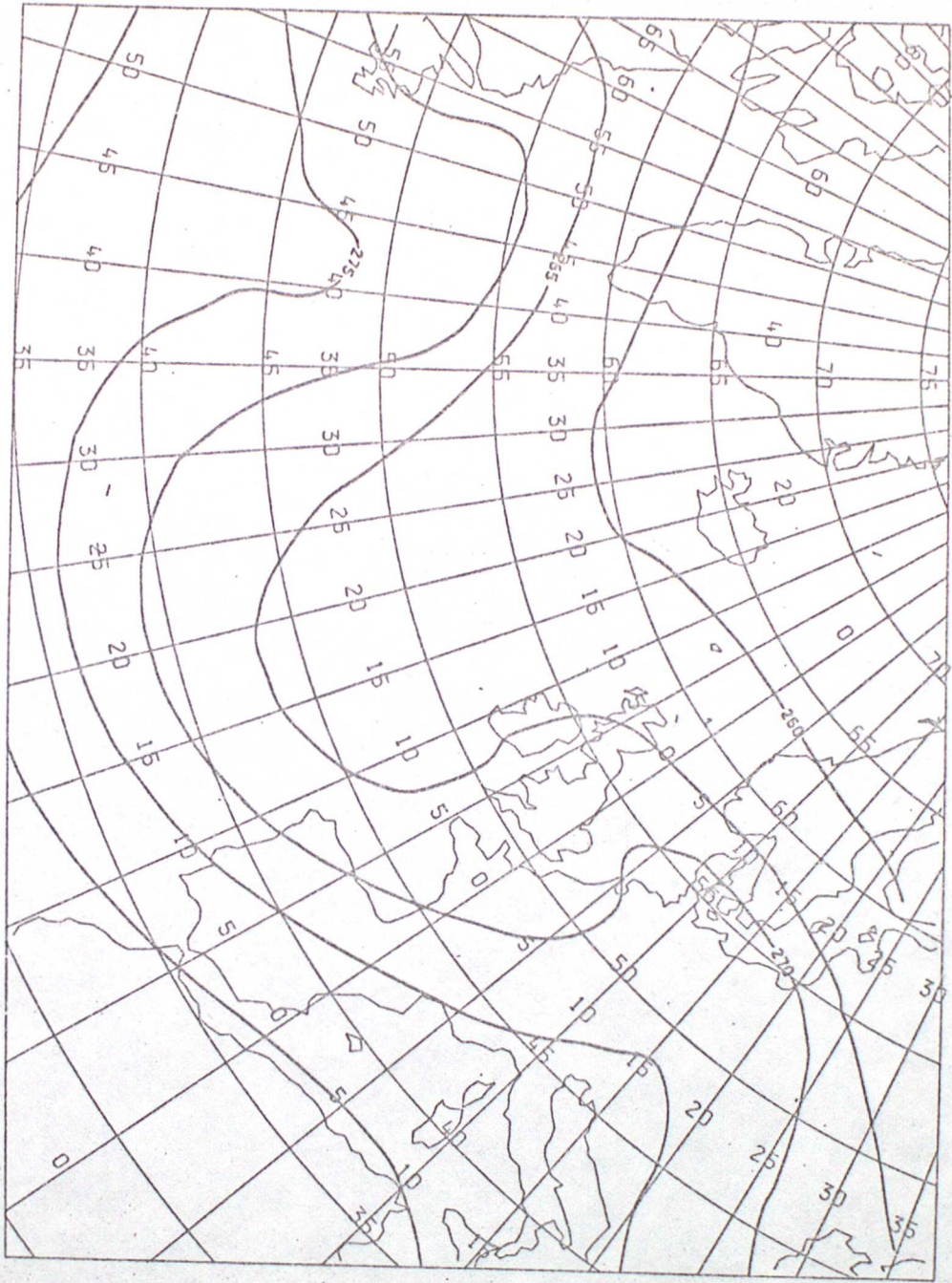
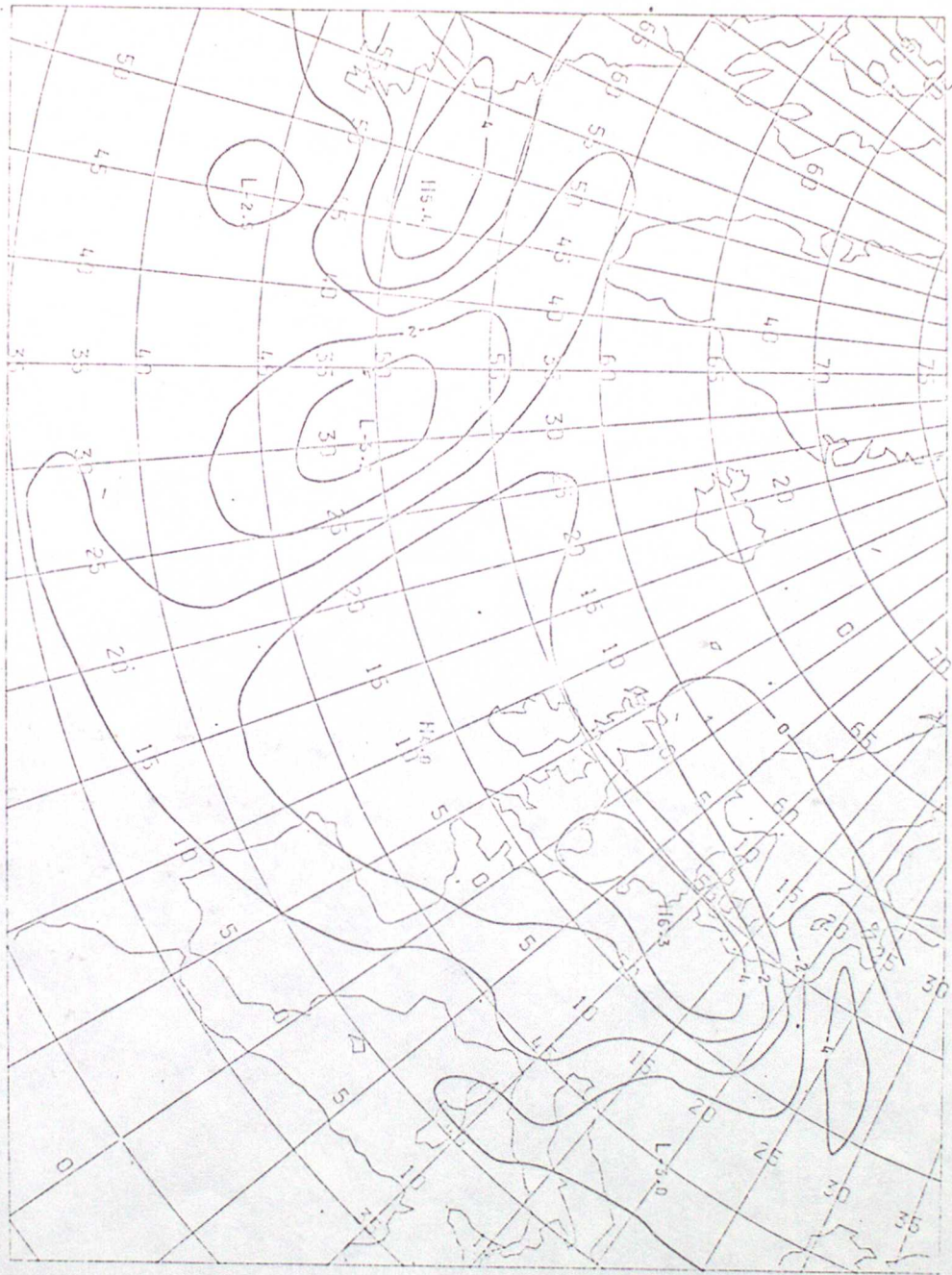
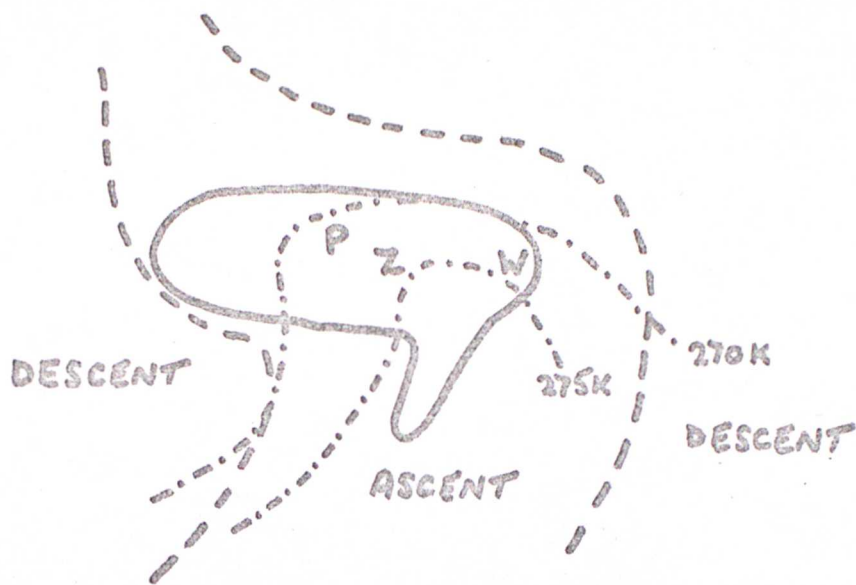


Fig 9e





- 1000mb vorticity = $2 \times 10^{-5} \text{ s}^{-1}$
- - - - - 550mb vertical velocity = 0
- . . . - 950mb temperature = 270K or 275K

- P Minimum pressure
- Z Maximum cyclonic vorticity
- W Maximum rate of ascent

Fig 10

SIZE OF CROSS AT 950MB +

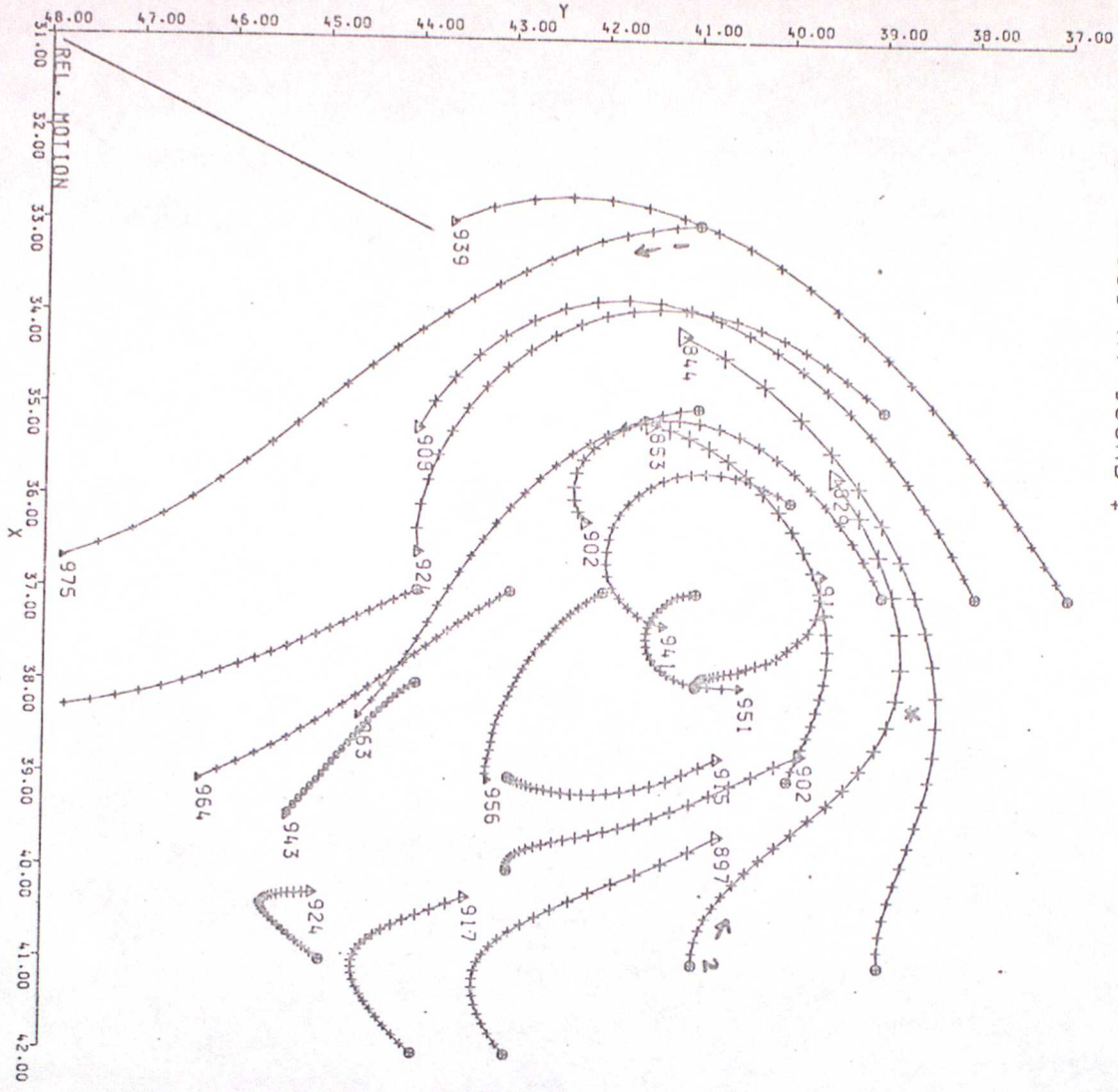


Fig 11a

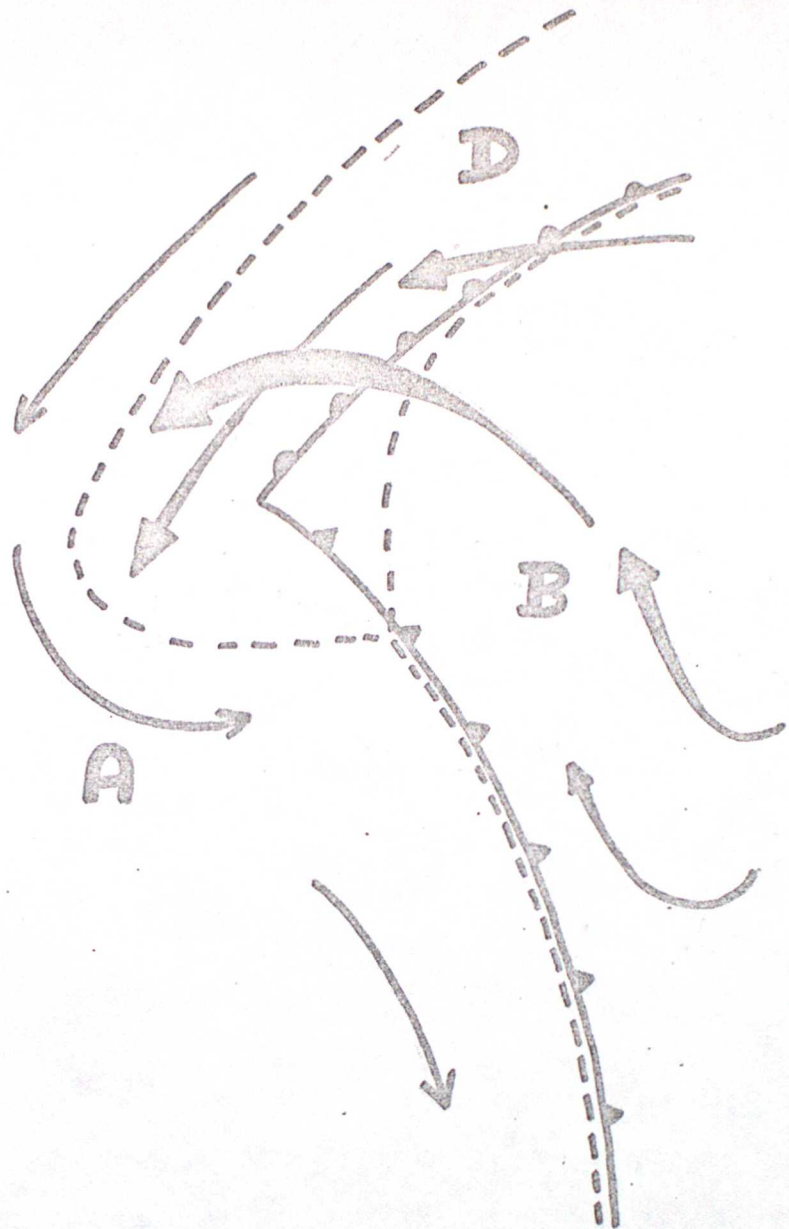


Fig 116

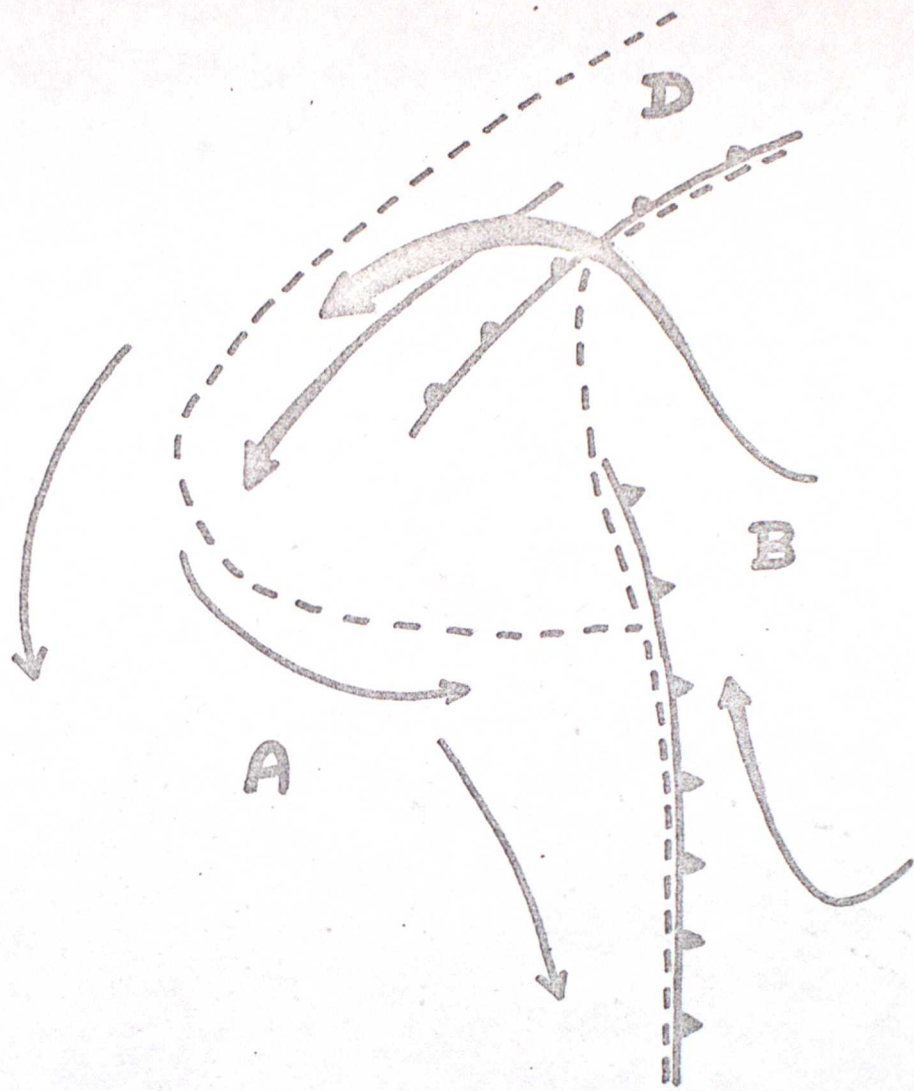


Fig. 126

SIZE OF CROSS AT 950MB +

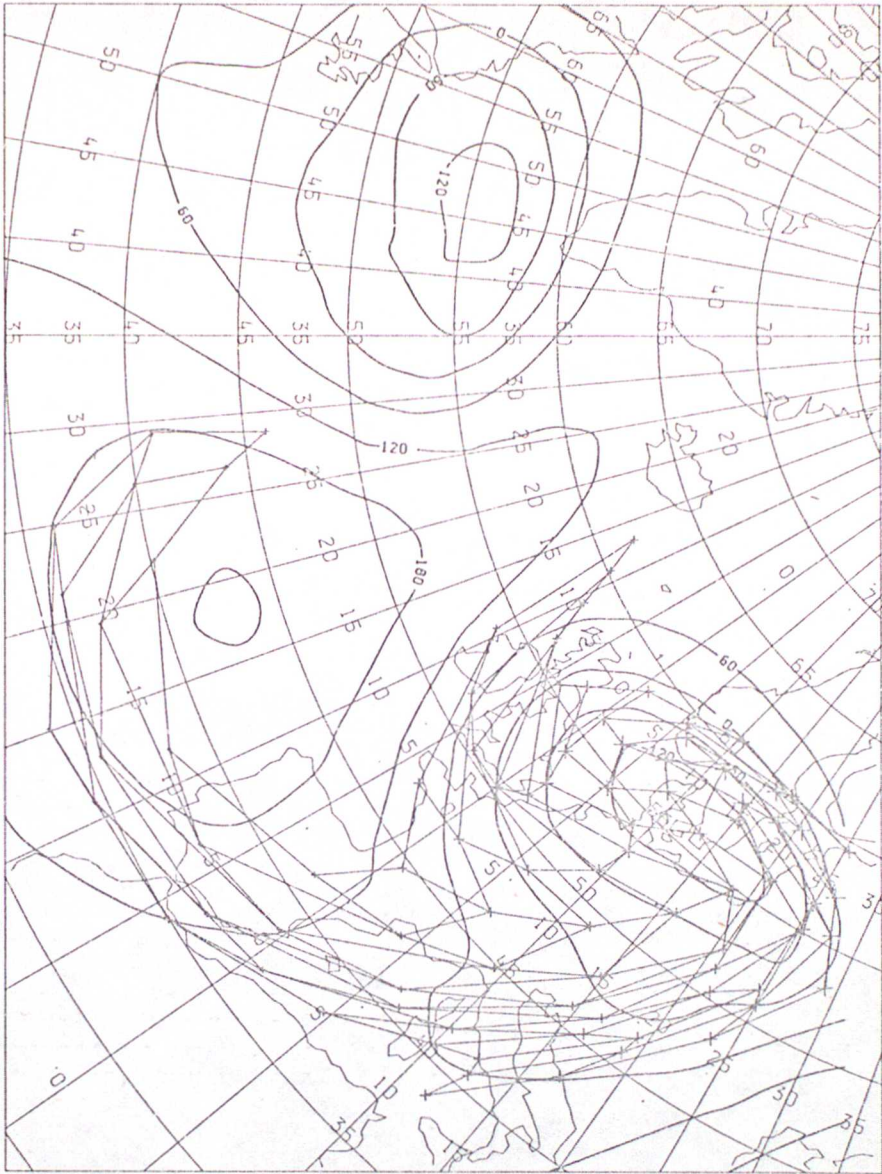


Fig 13

INITIAL POSITION (33,41,950)

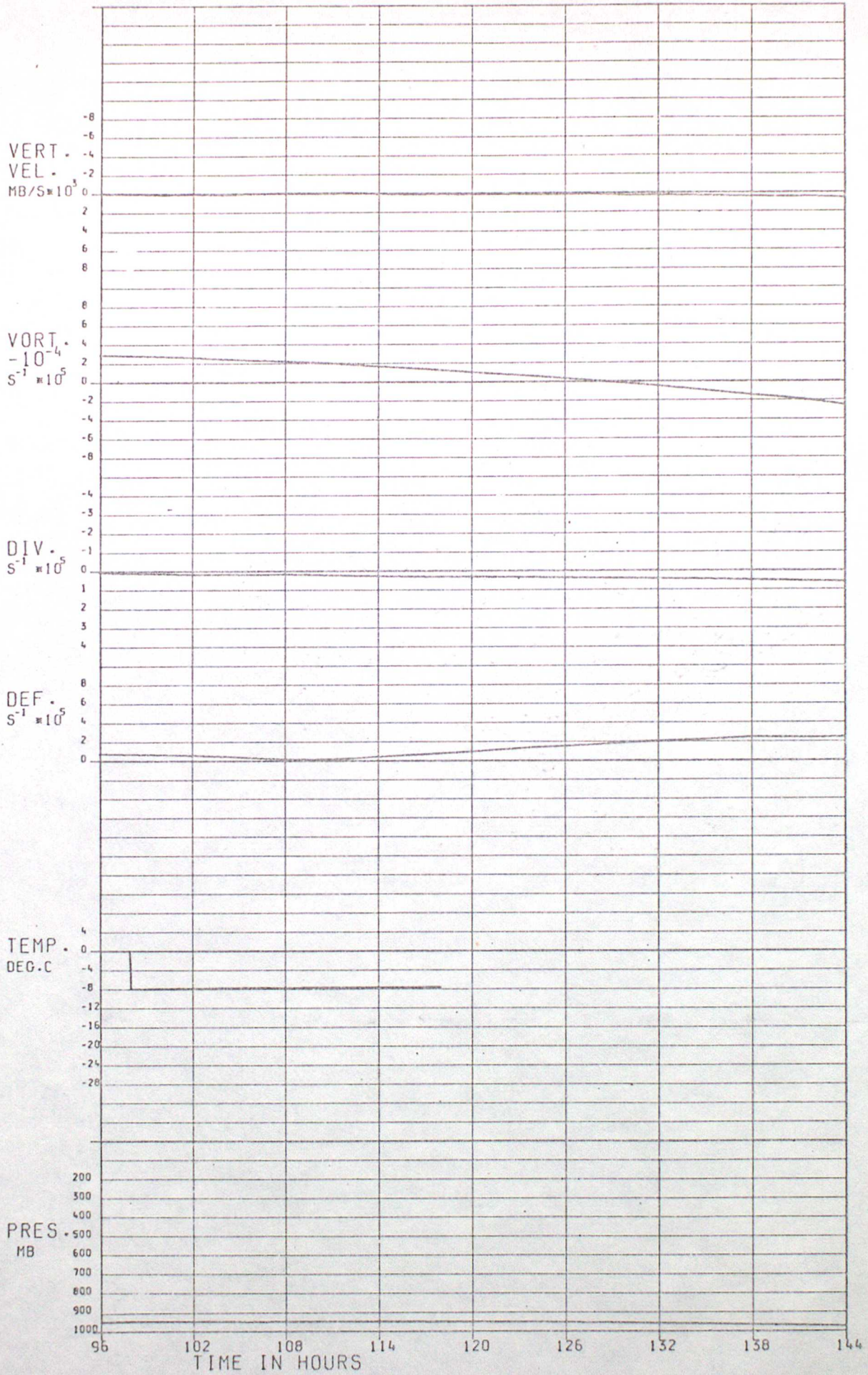


Fig 14a

INITIAL POSITION (41,41,950)

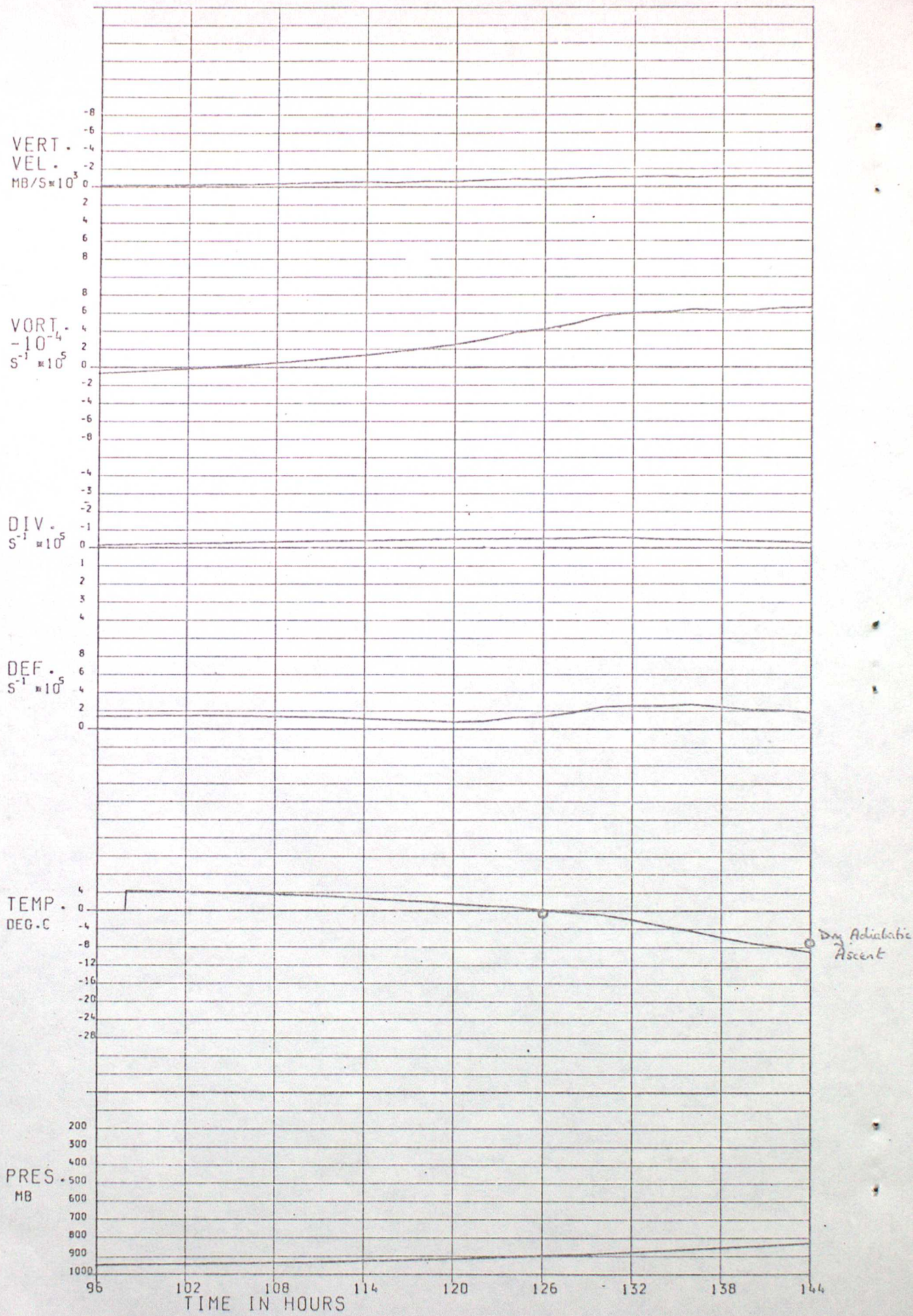


Fig 14b

INITIAL POSITION (41, 41, 950)

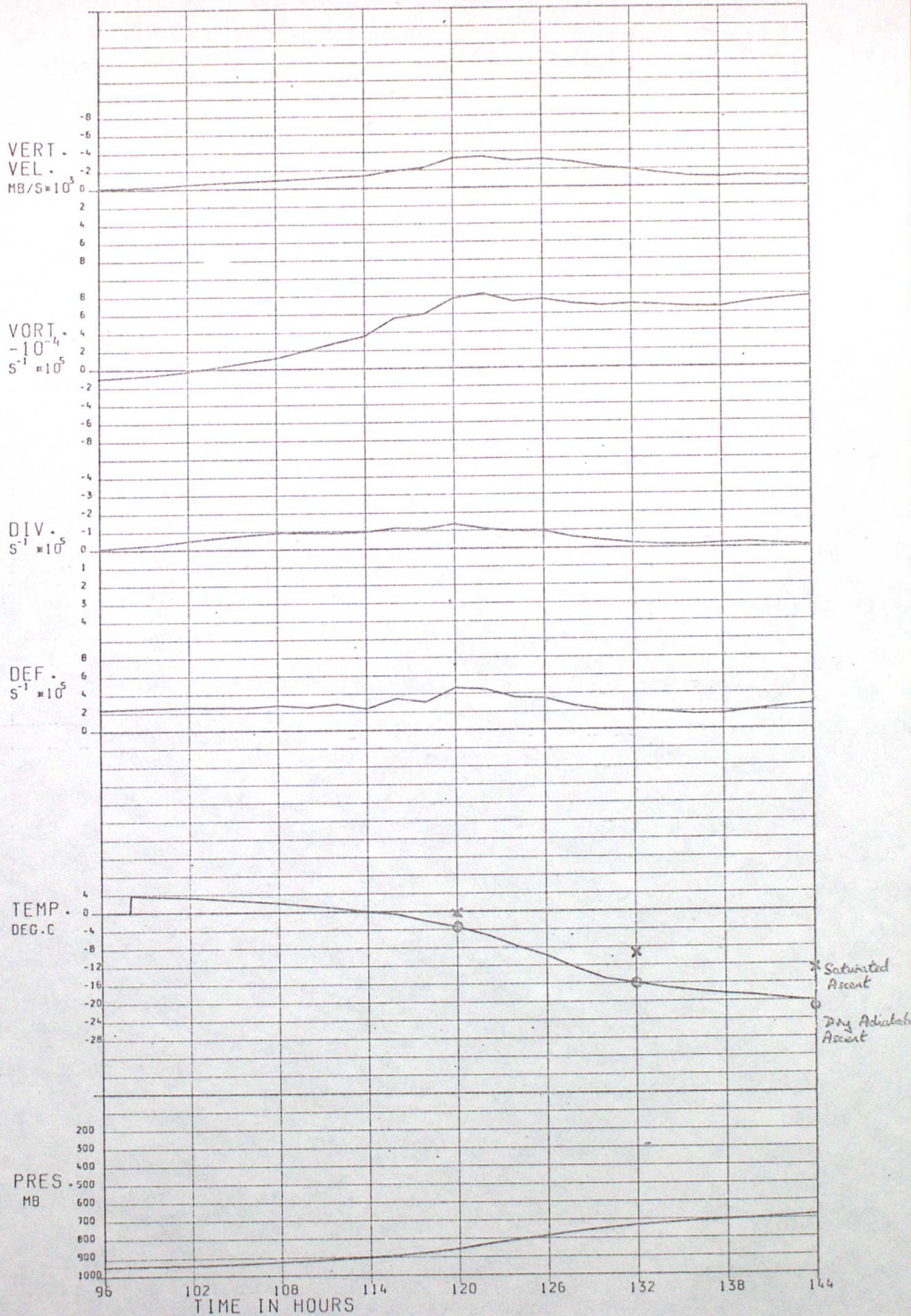


Fig 14c

SIZE OF CROSS AT 750MB +

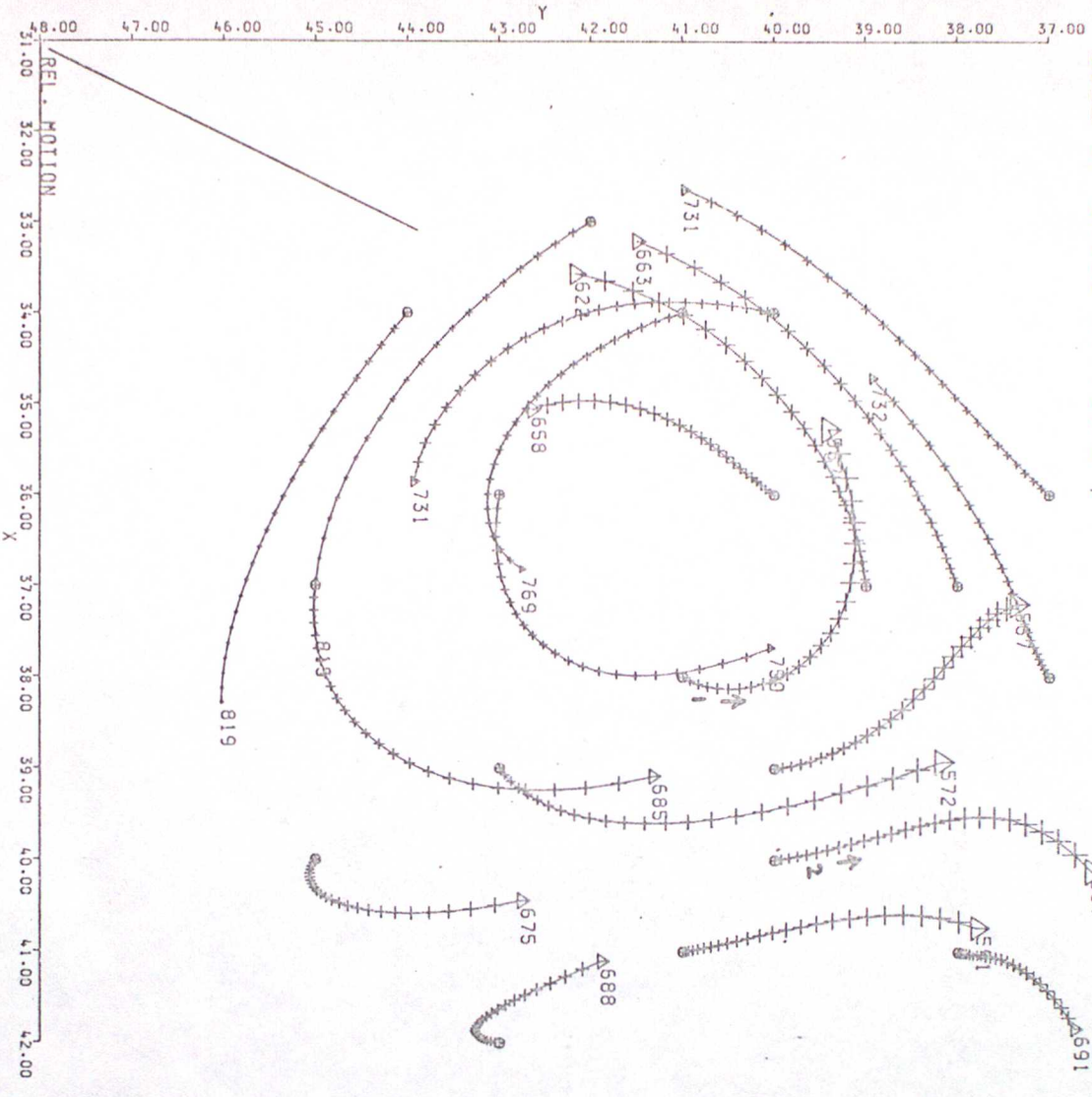


Fig 15a

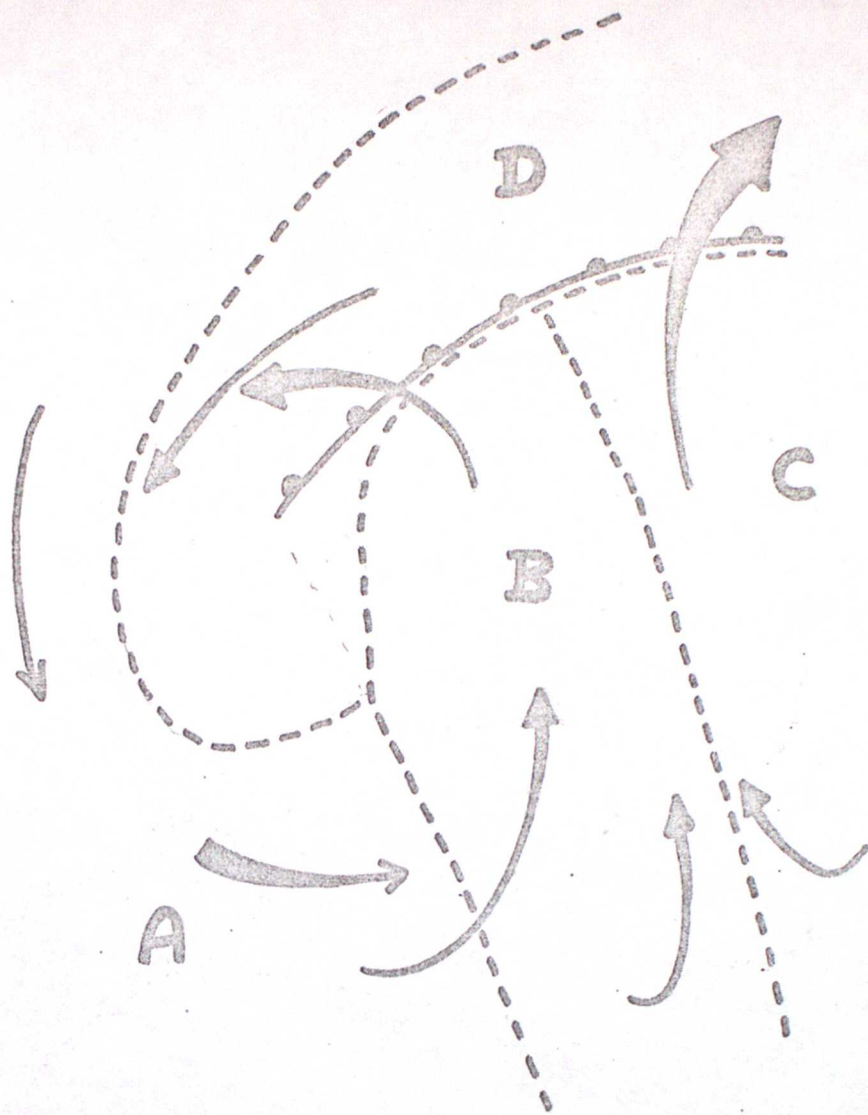


Fig 156

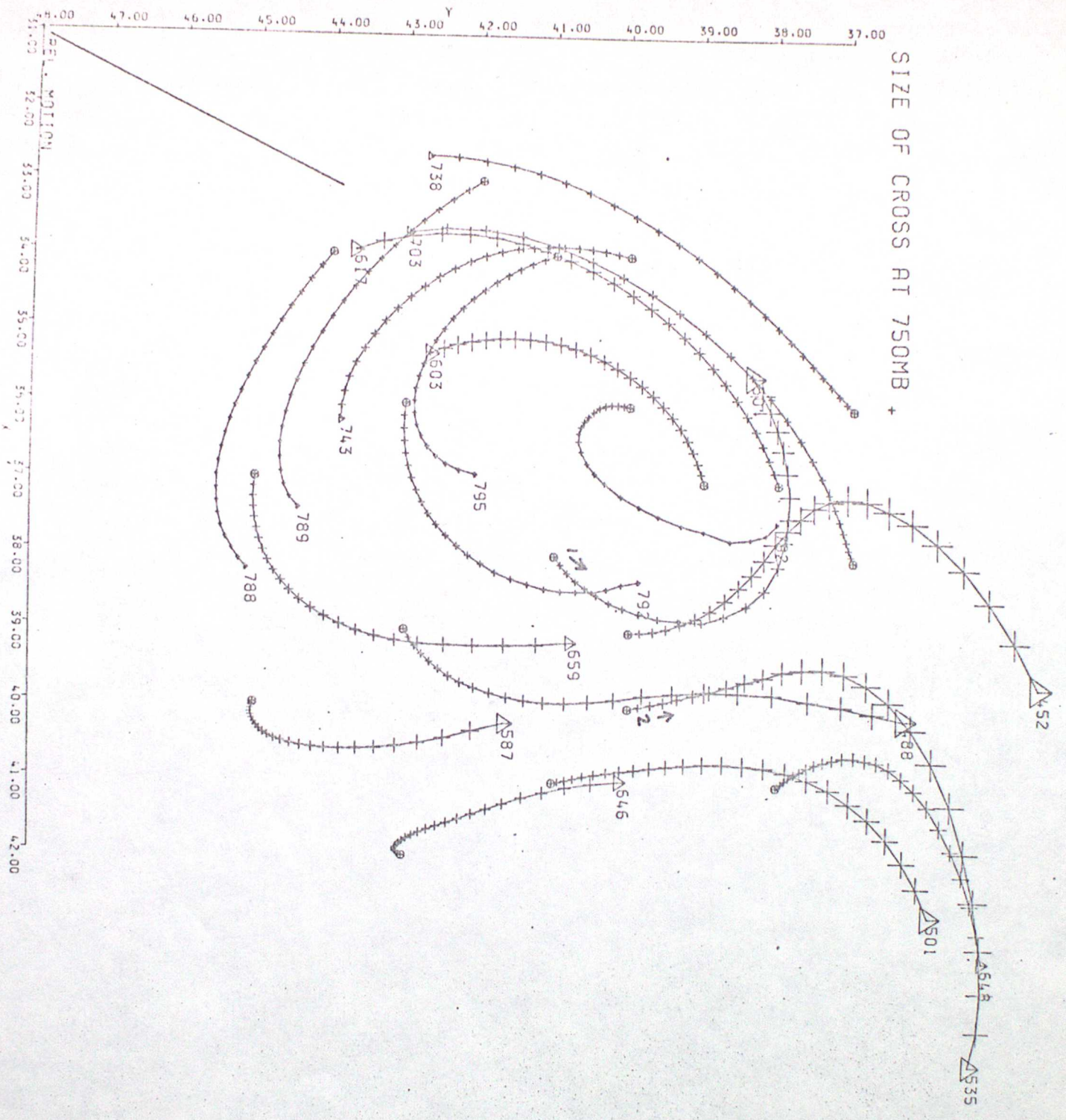


Fig 16a

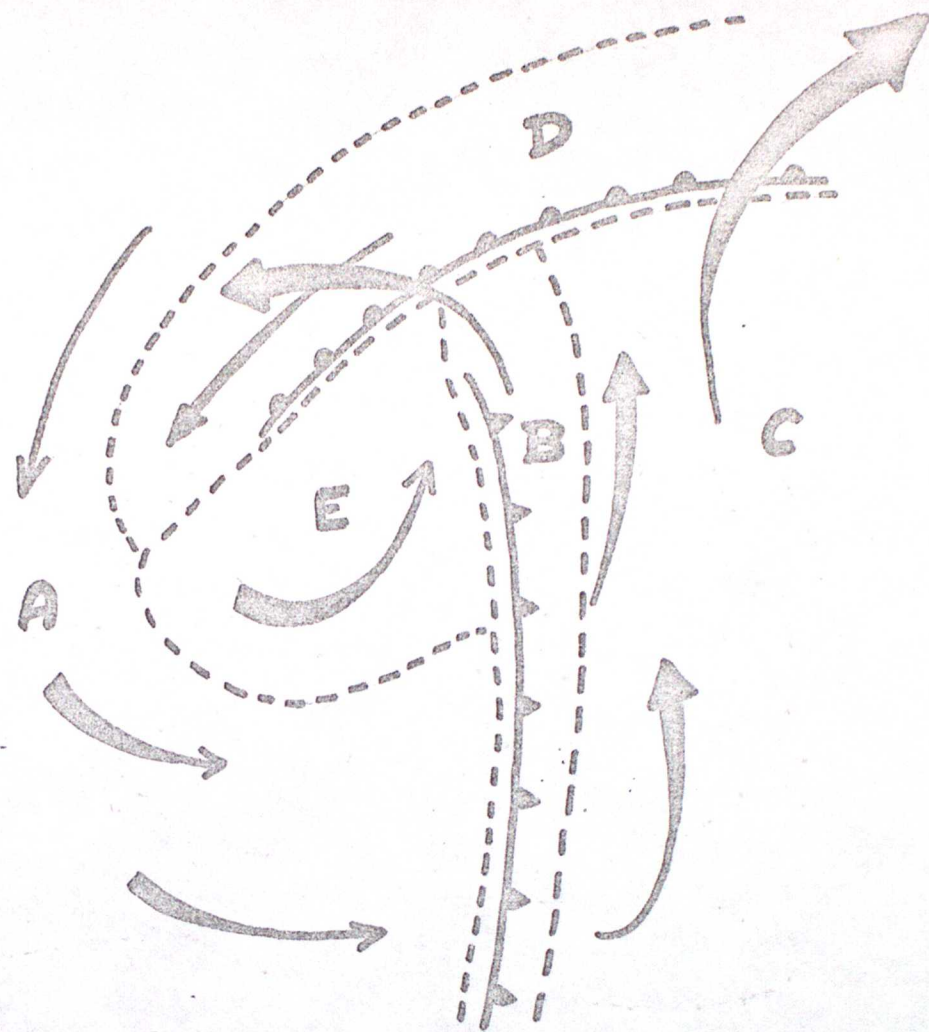


Fig 166

SIZE OF CROSS AT 750MB +

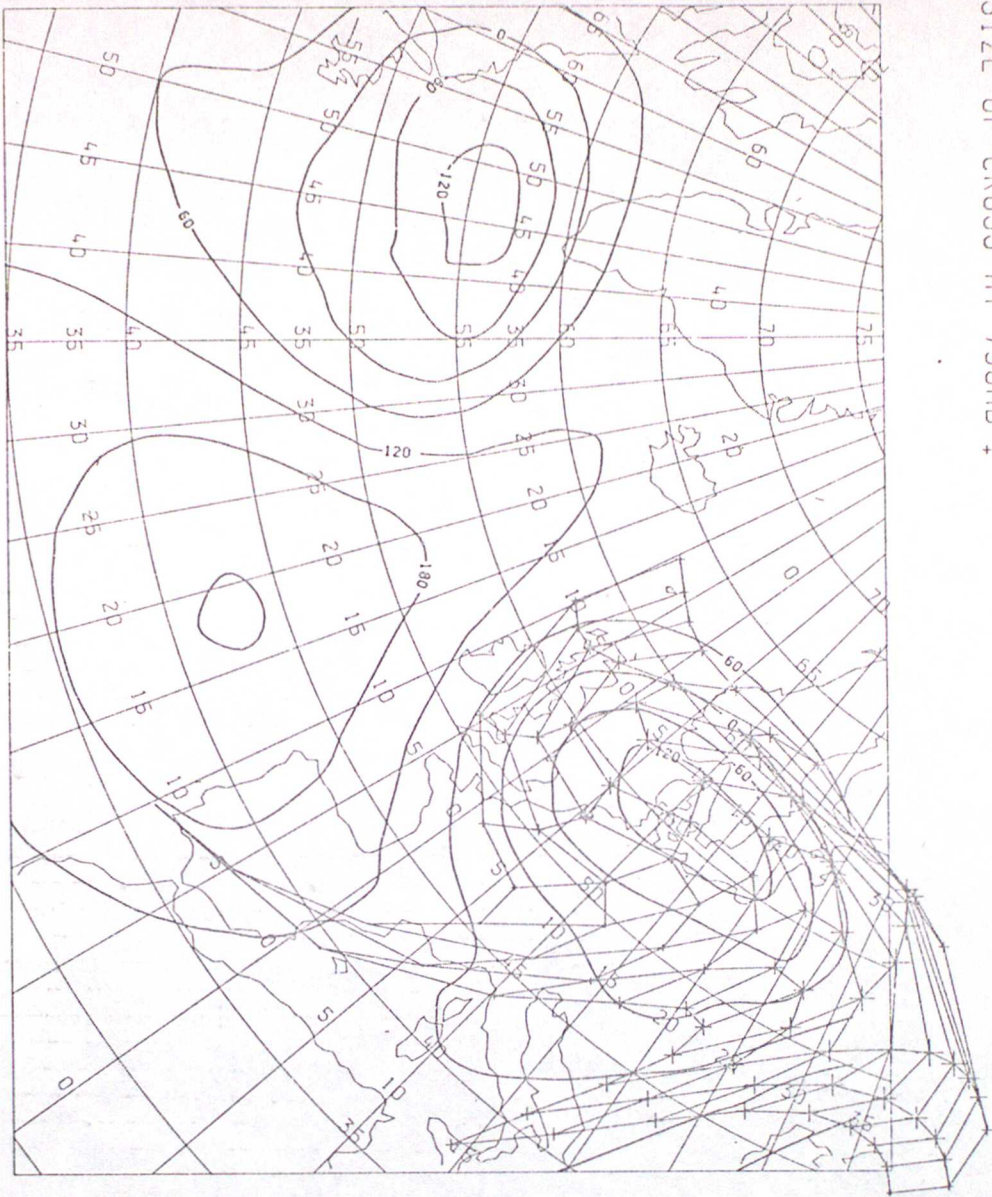


Fig. 17

INITIAL POSITION (38,41,750)

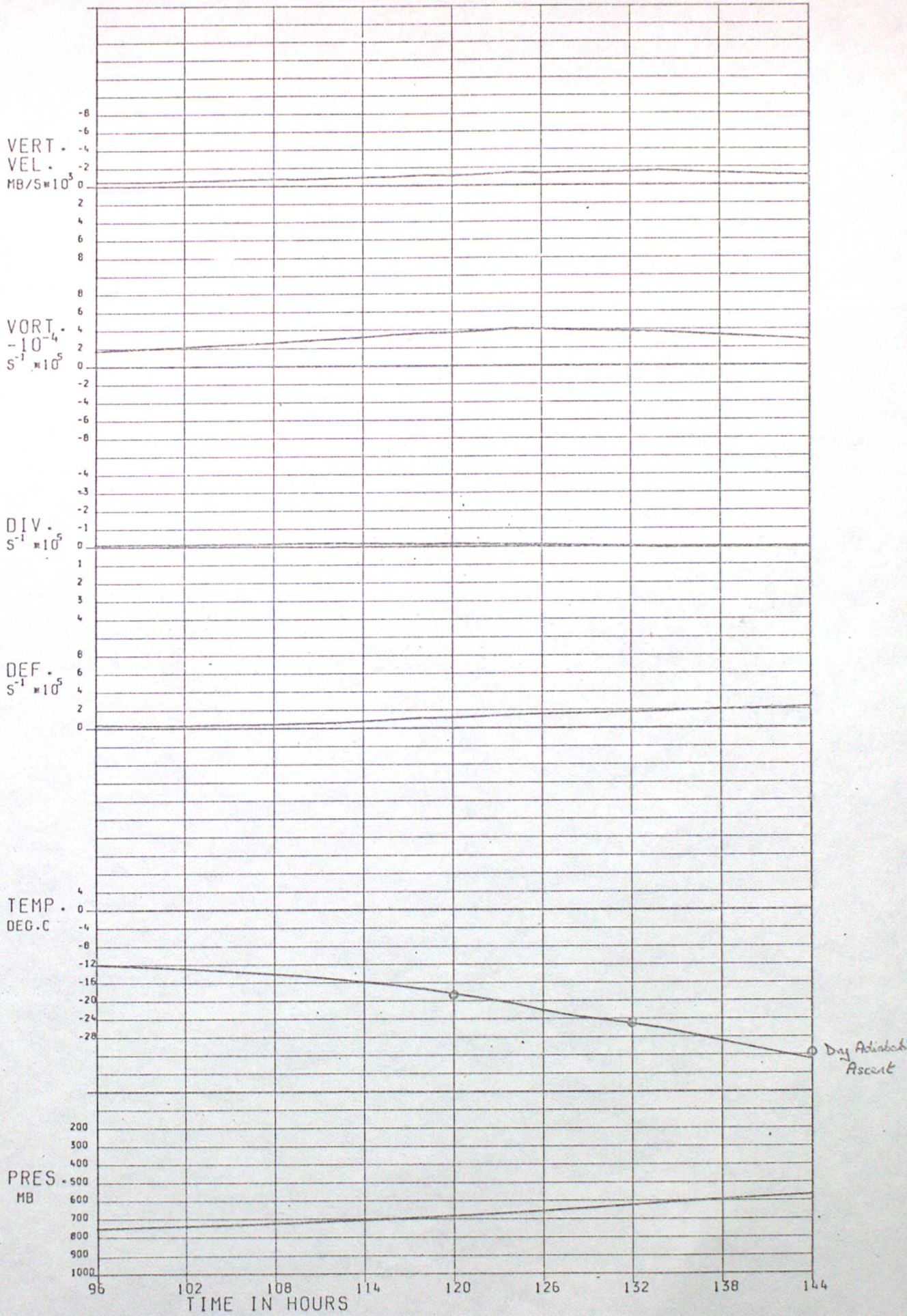


Fig 18a

IN TIAL POSITION (40, 40, 750)

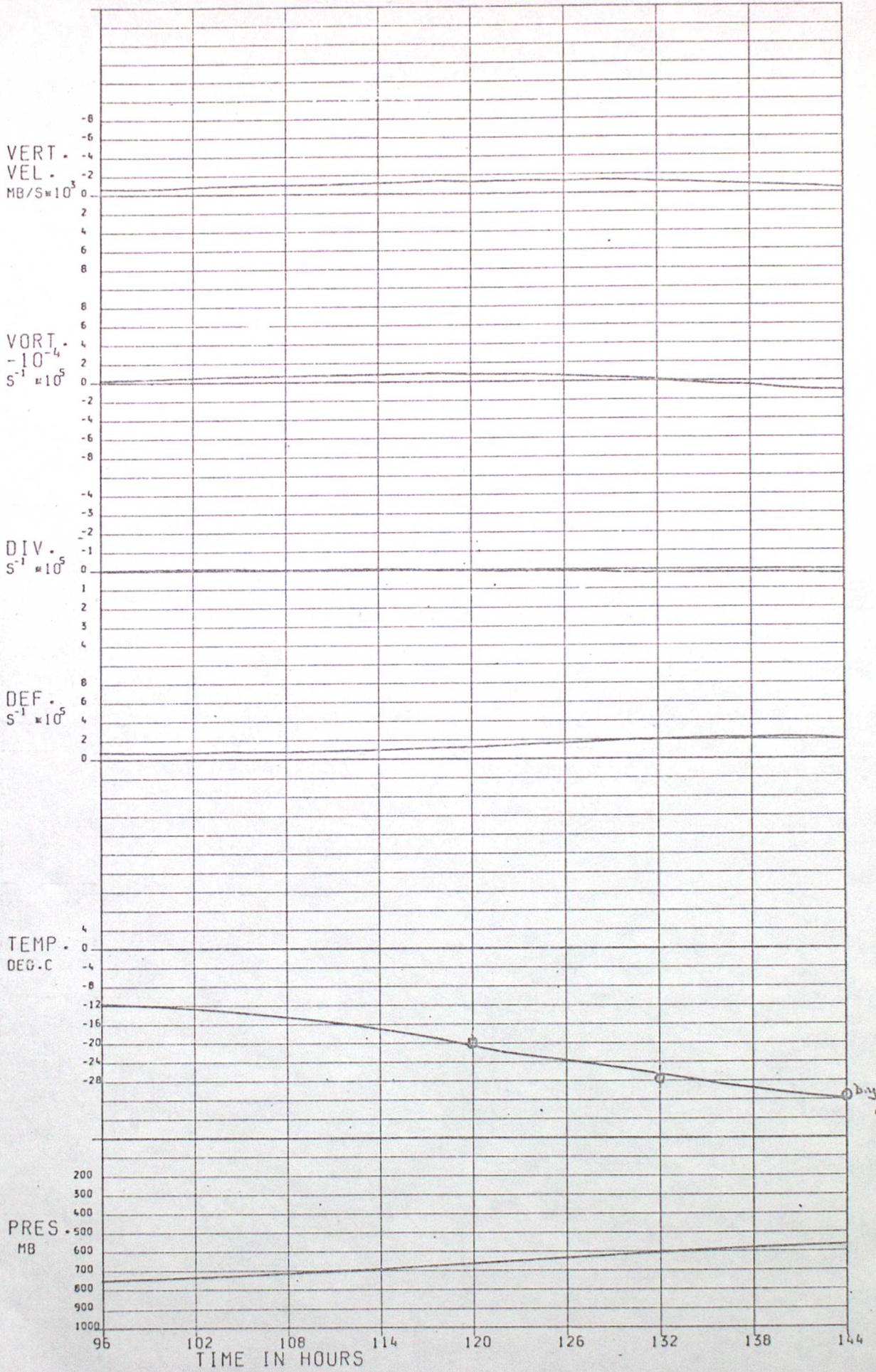


Fig 186

INITIAL POSITION (38,41,750)

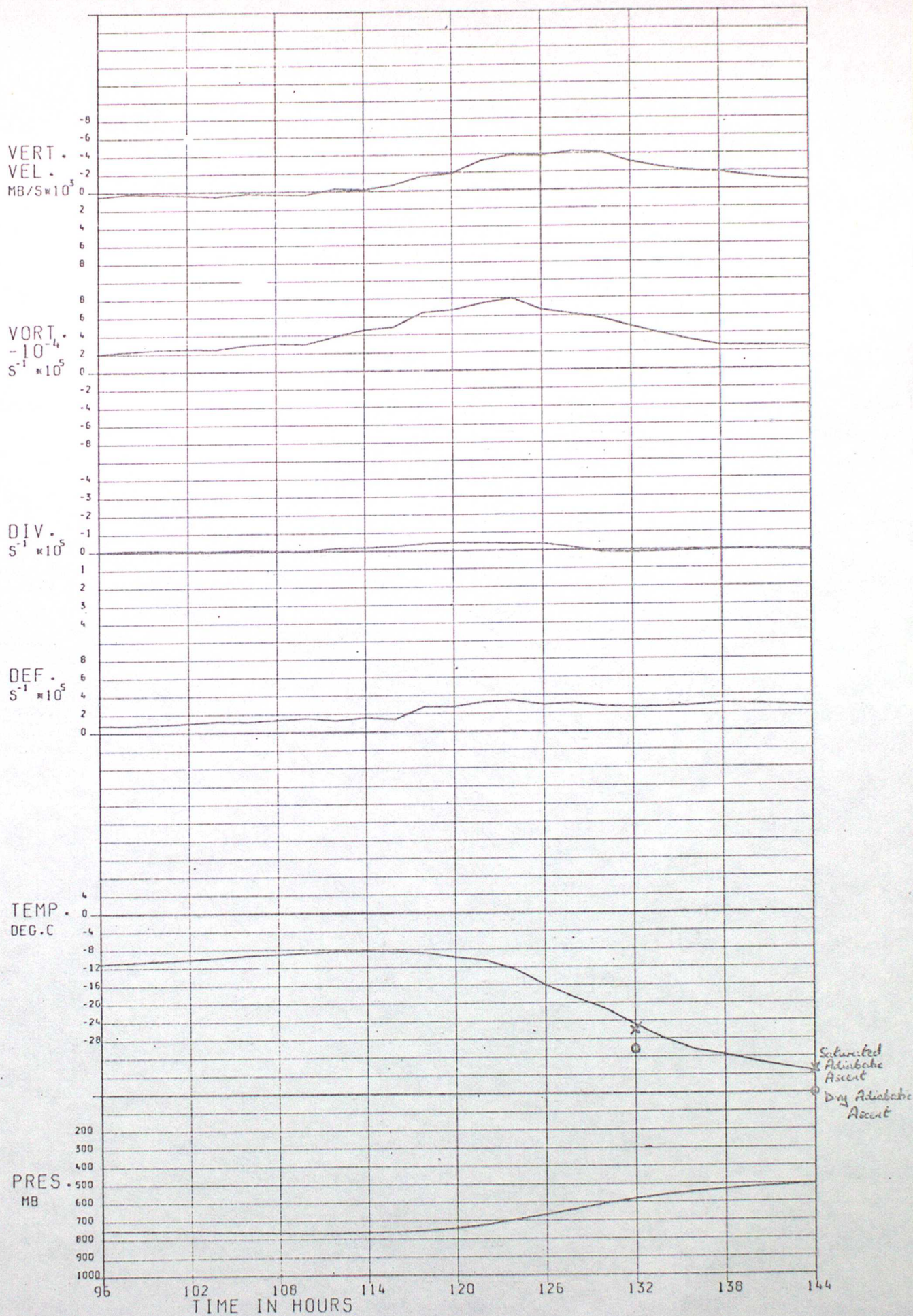


Fig 18c

INITIAL POSITION (40, 40, 750)

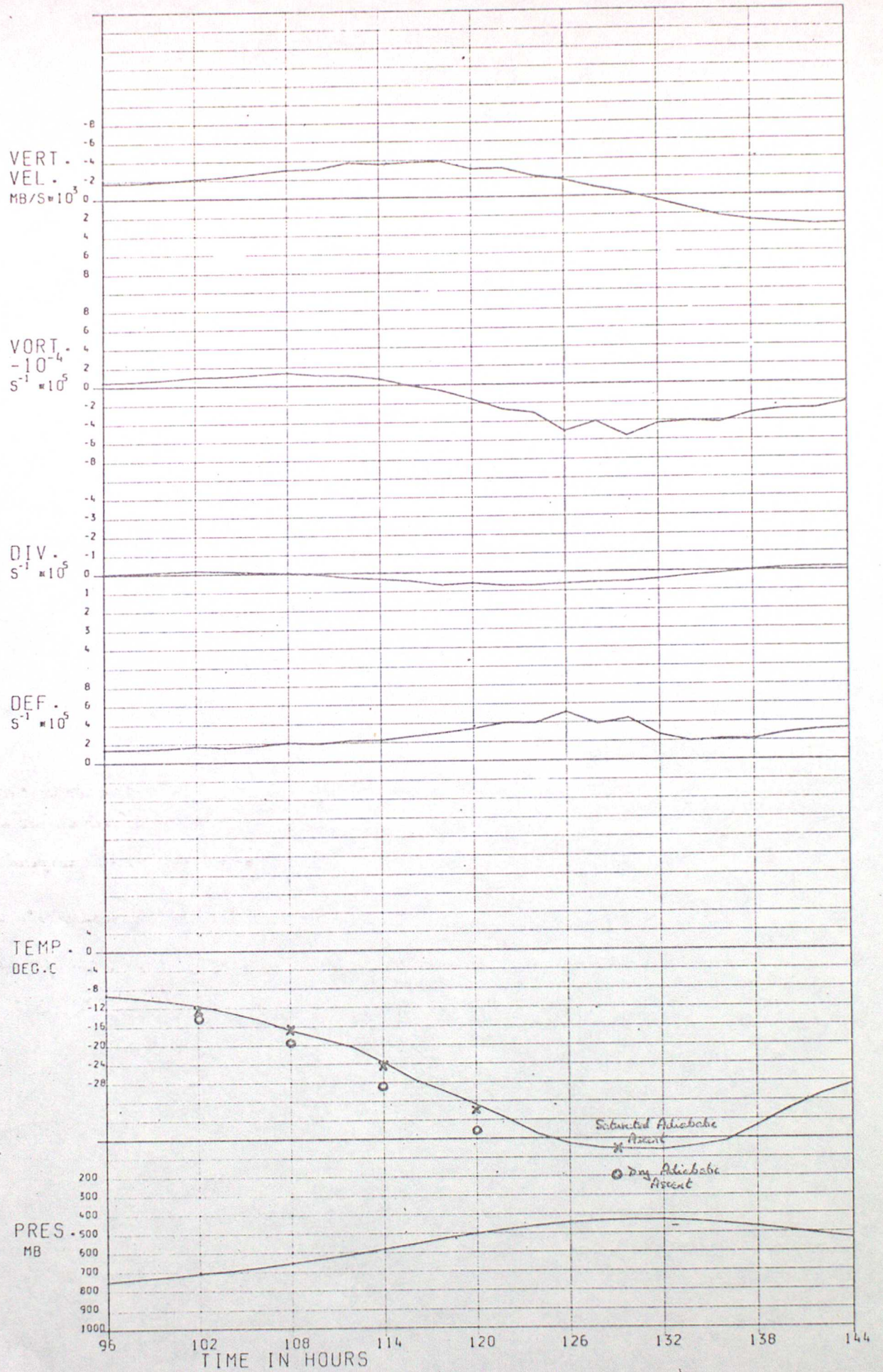
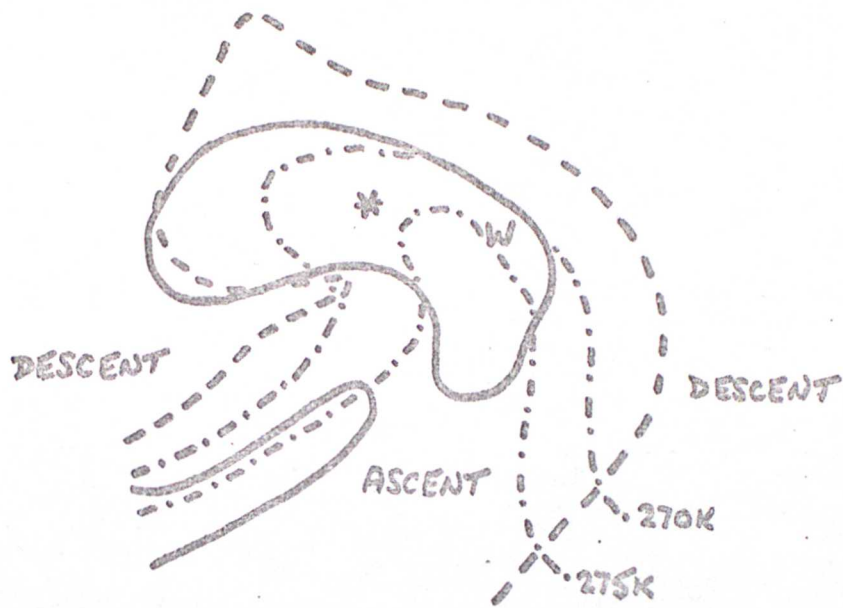


Fig 18d



- 1000 mb vorticity = $2 \times 10^{-5} \text{ s}^{-1}$
- - - - - 550 mb vertical velocity = 0
- 950 mb temperature = 270K or 275K
- W Maximum rate of ascent
- * { Minimum pressure
Maximum cyclonic vorticity

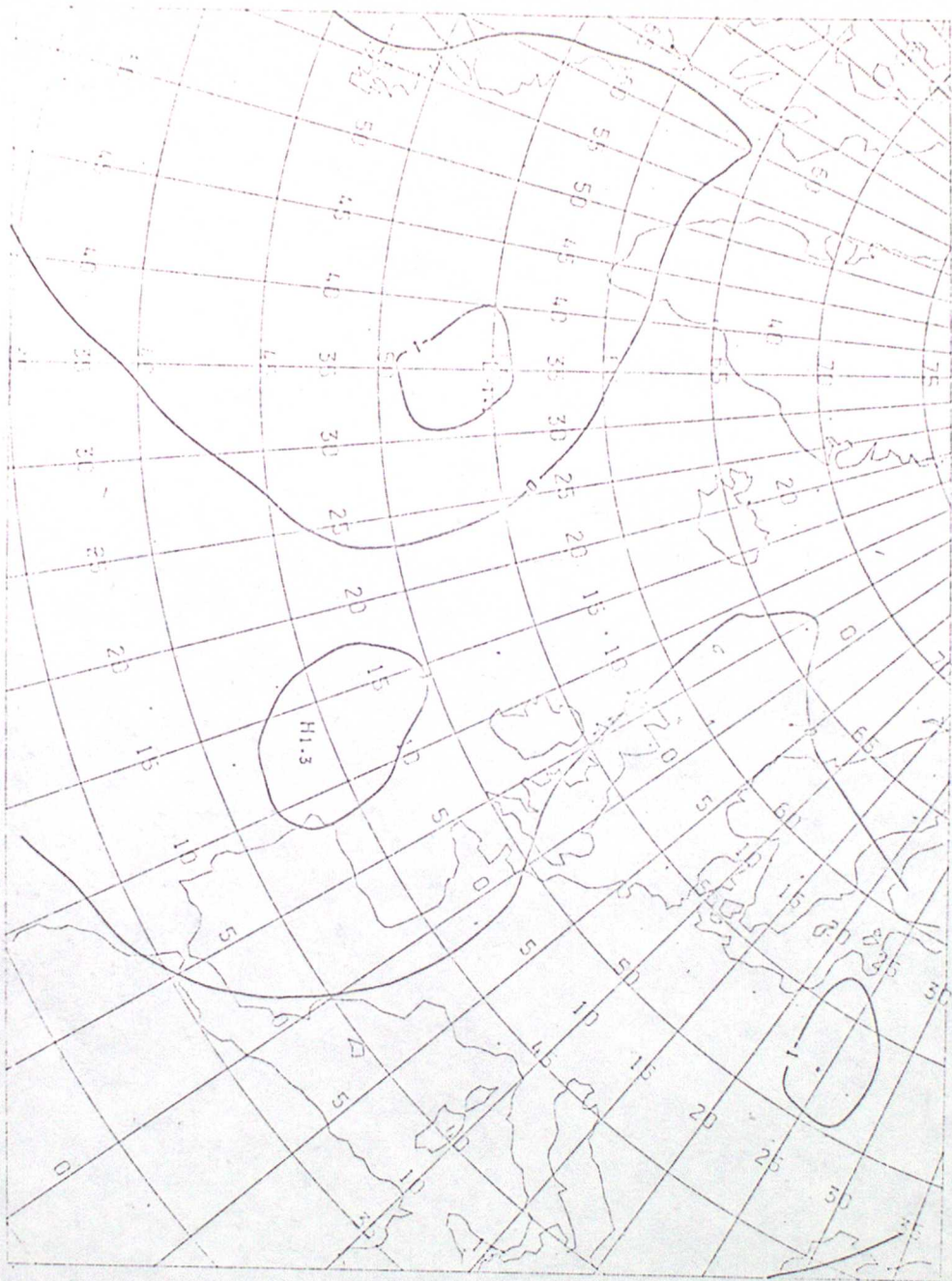


Fig 20a

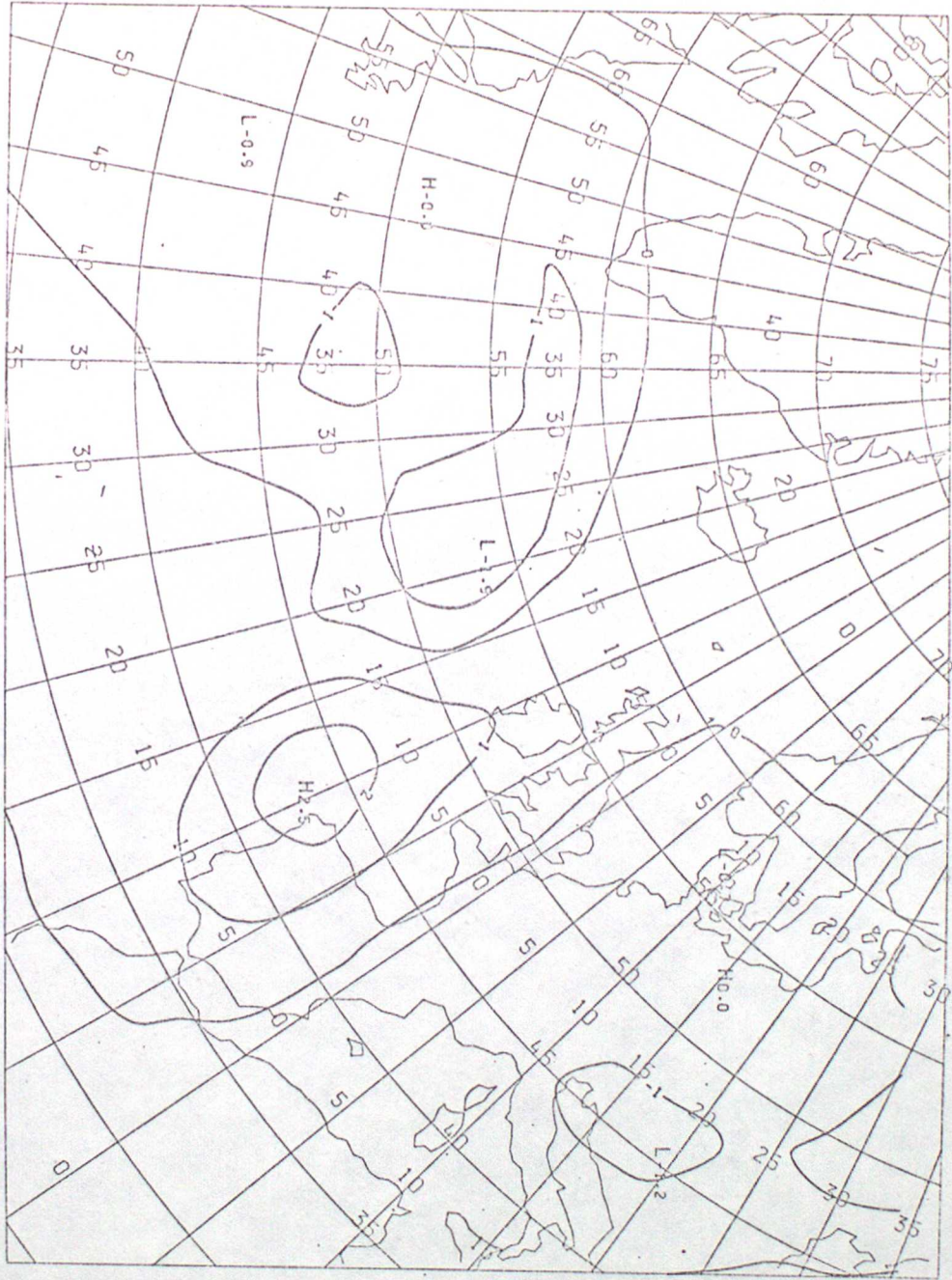


Fig 206

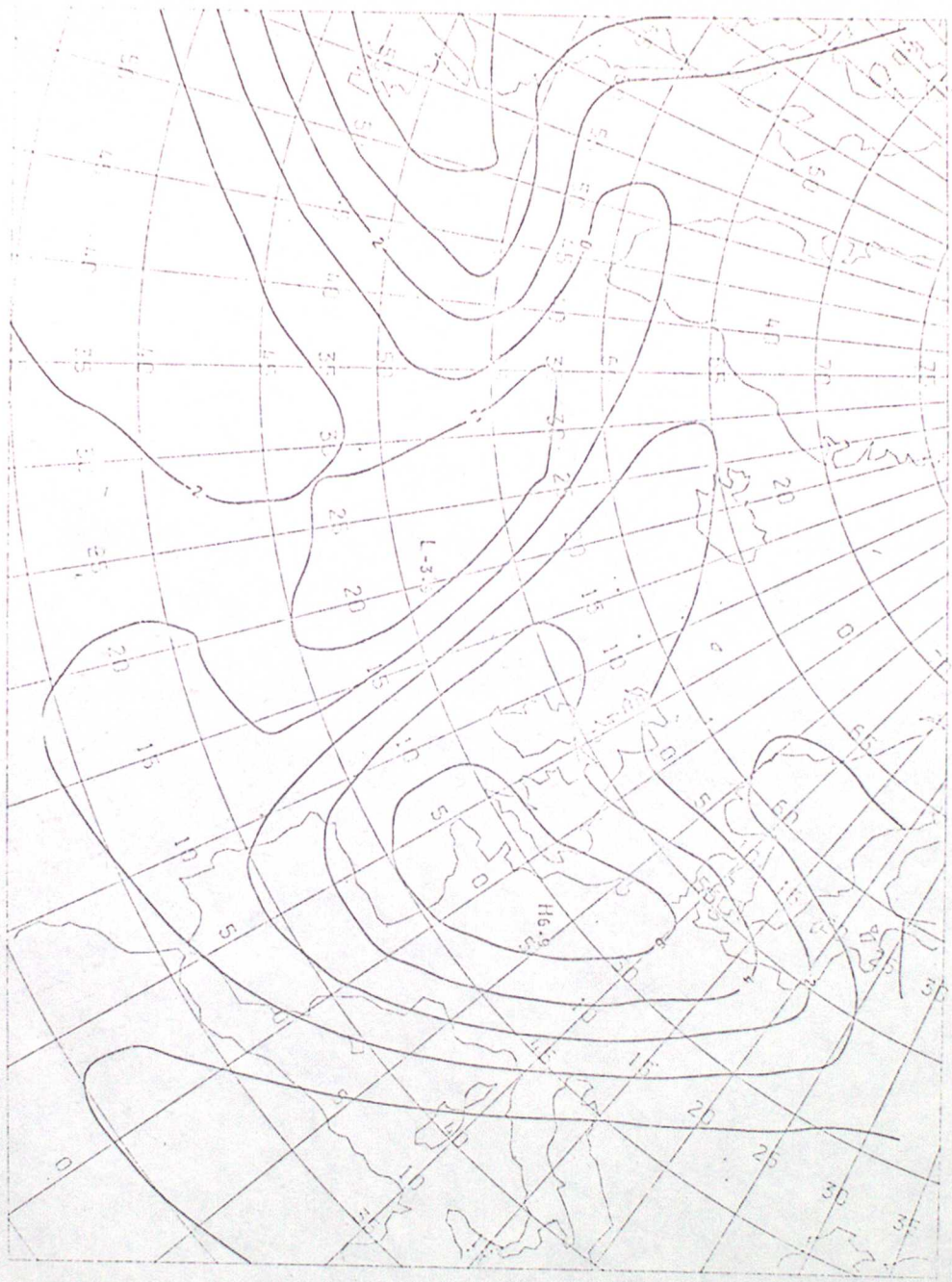


Fig 20c



Fig 20d

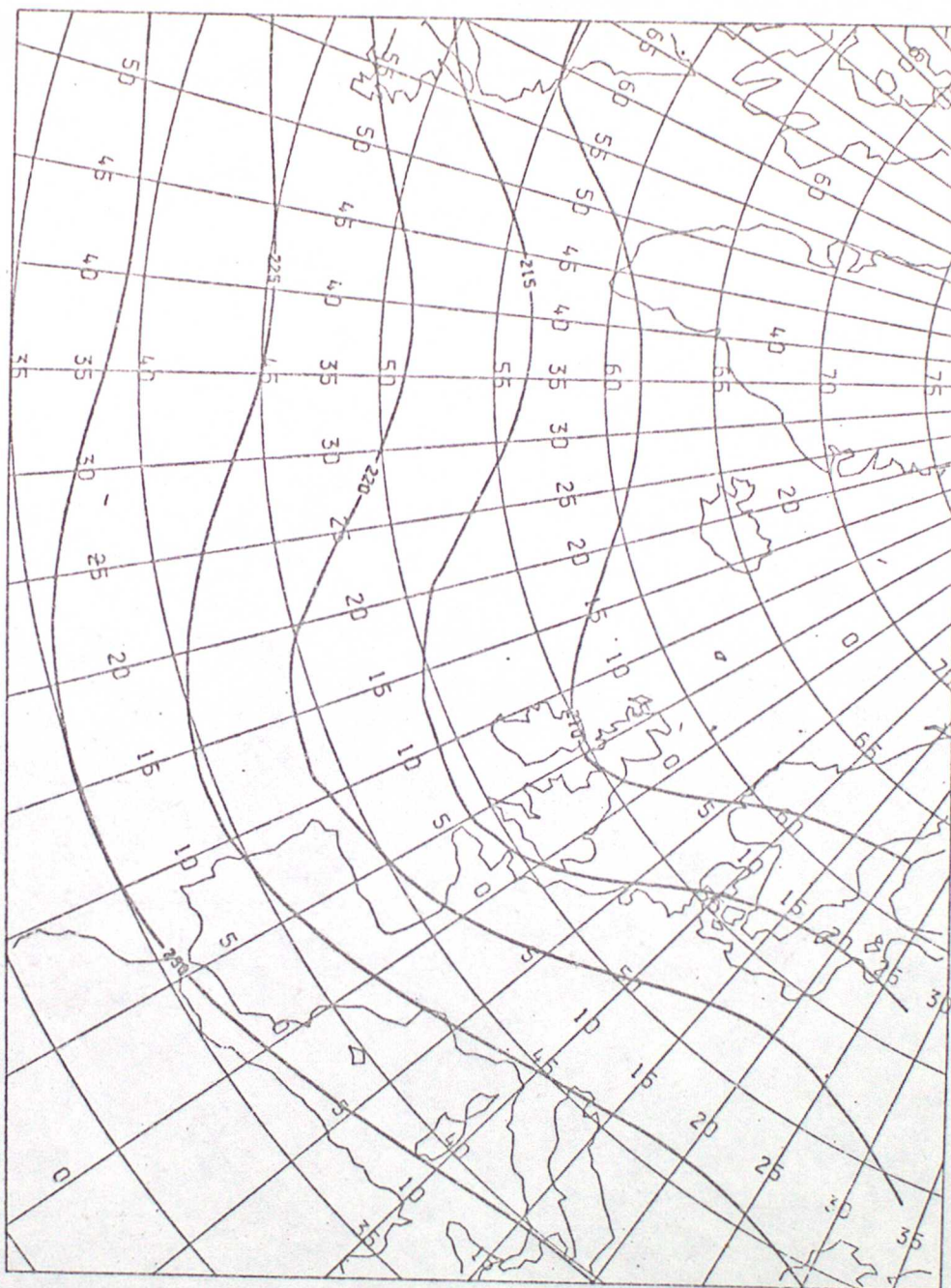


Fig 20e

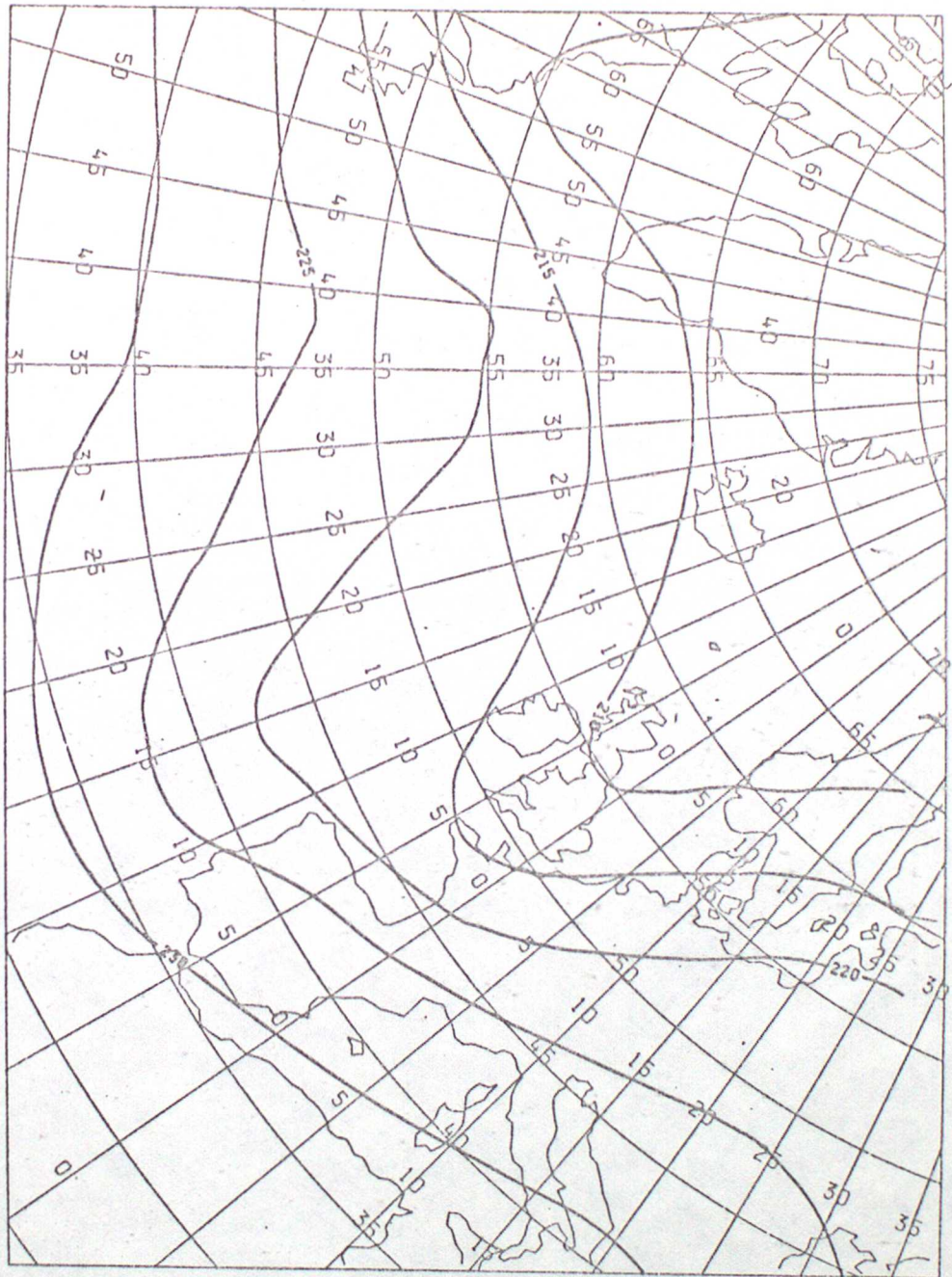


Fig 20f

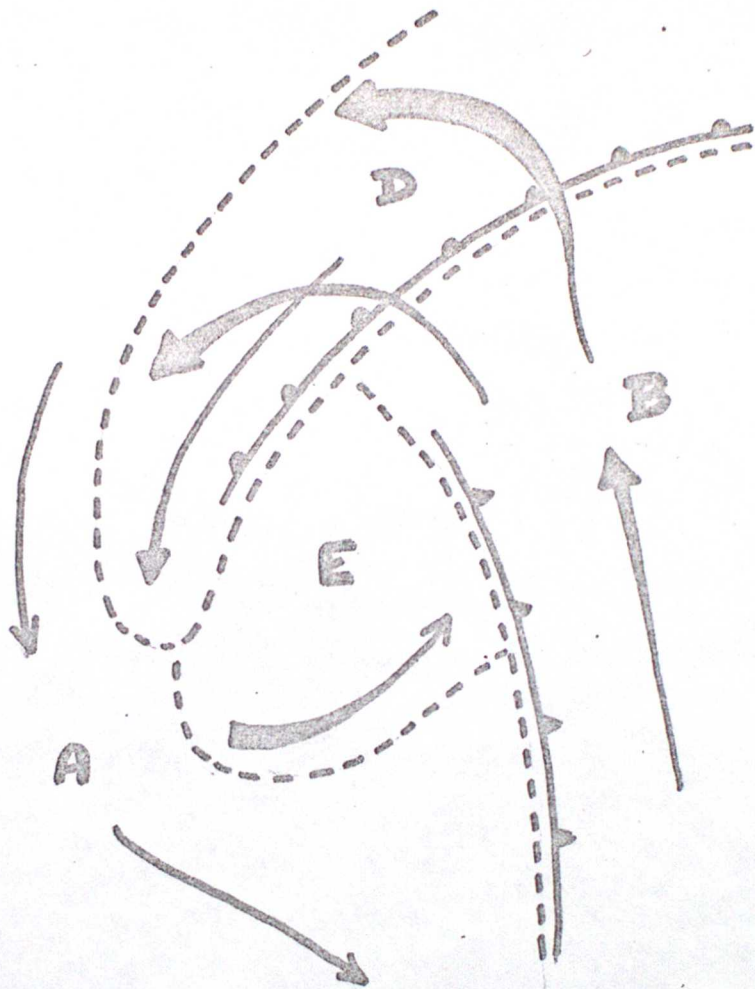


Fig 216

SIZE OF CROSS AT 750MB

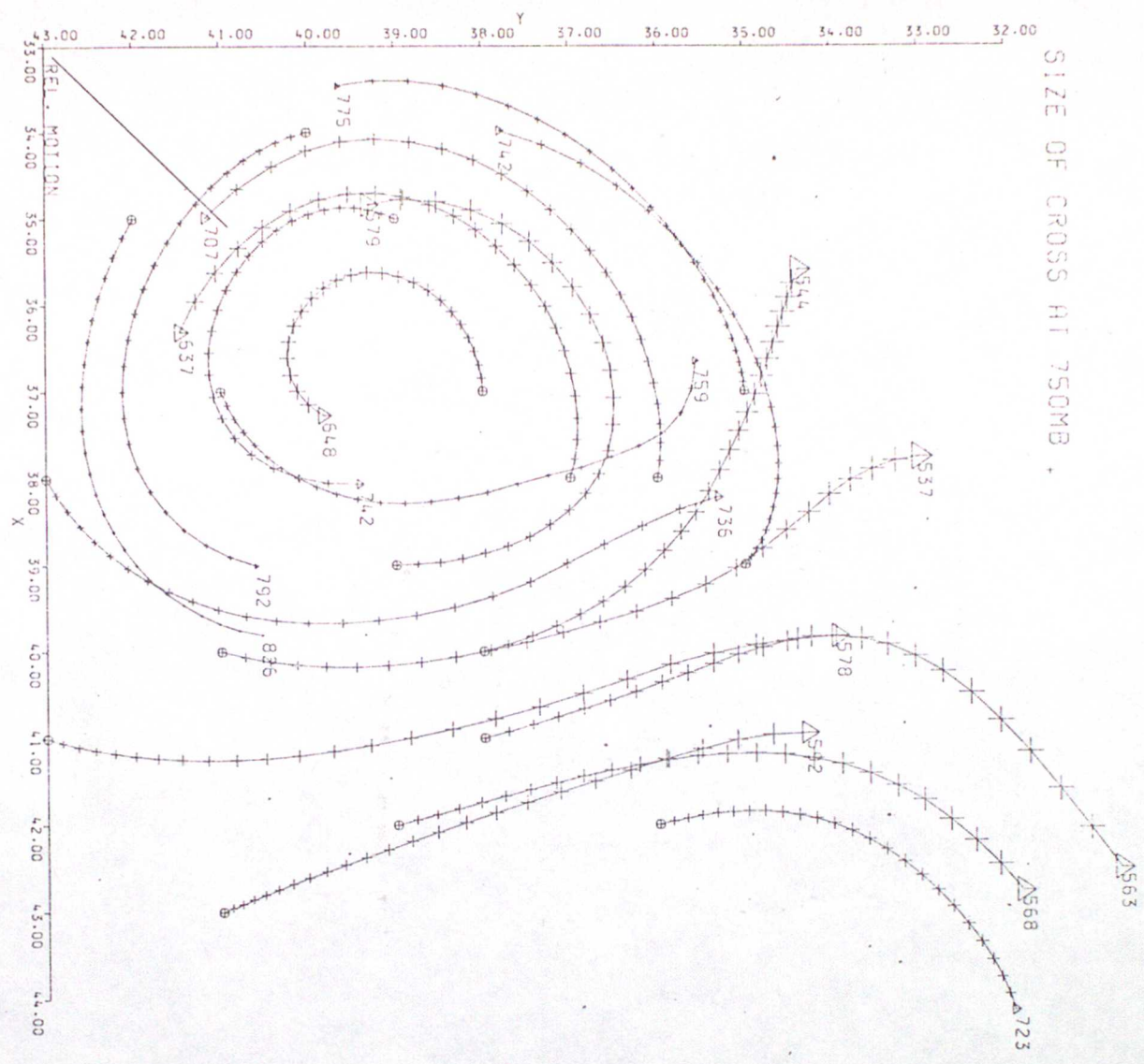


Fig. 22a

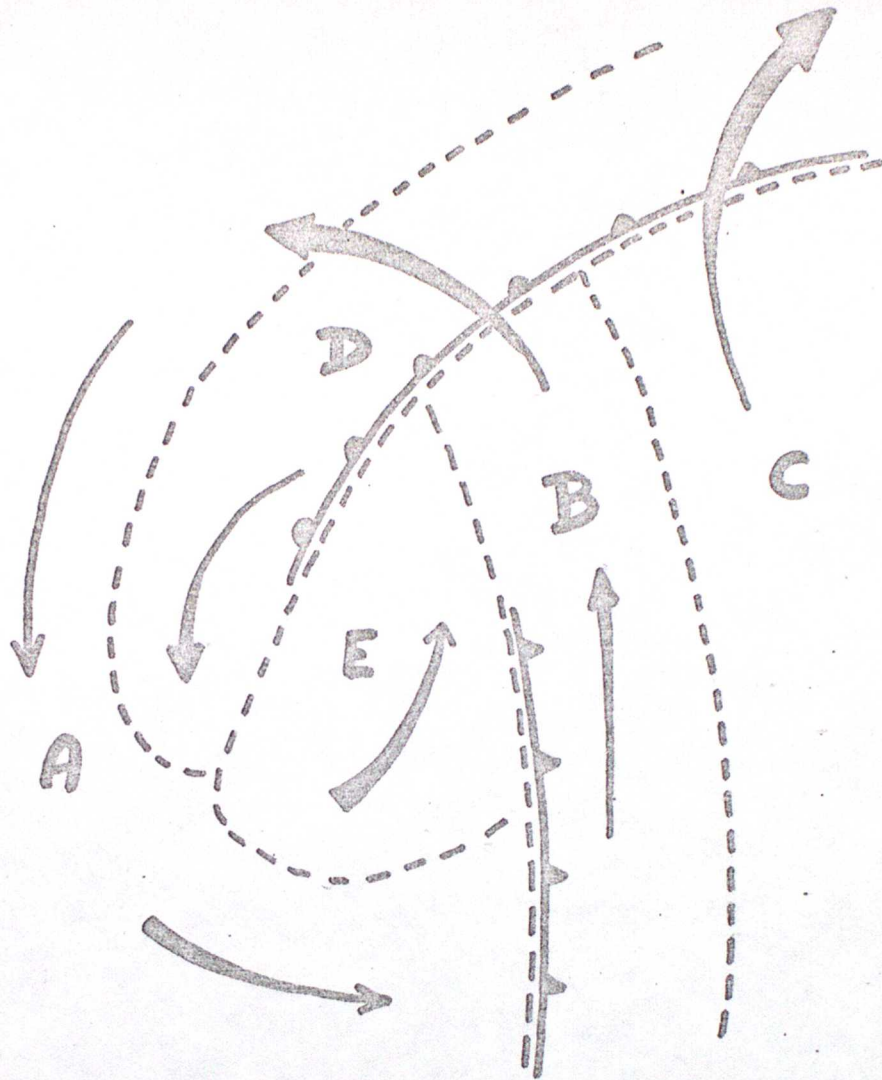


Fig 226

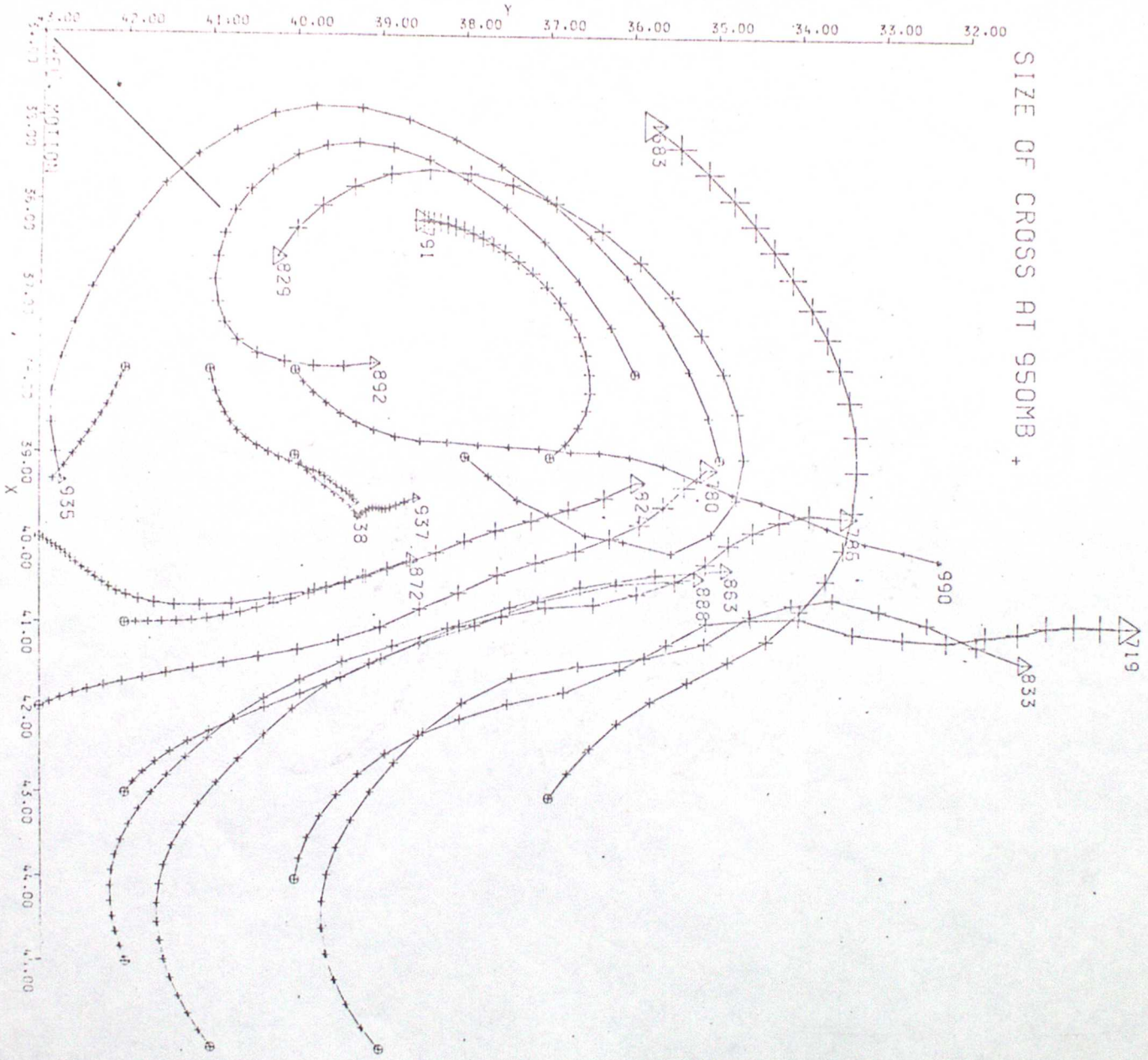


Fig 23a

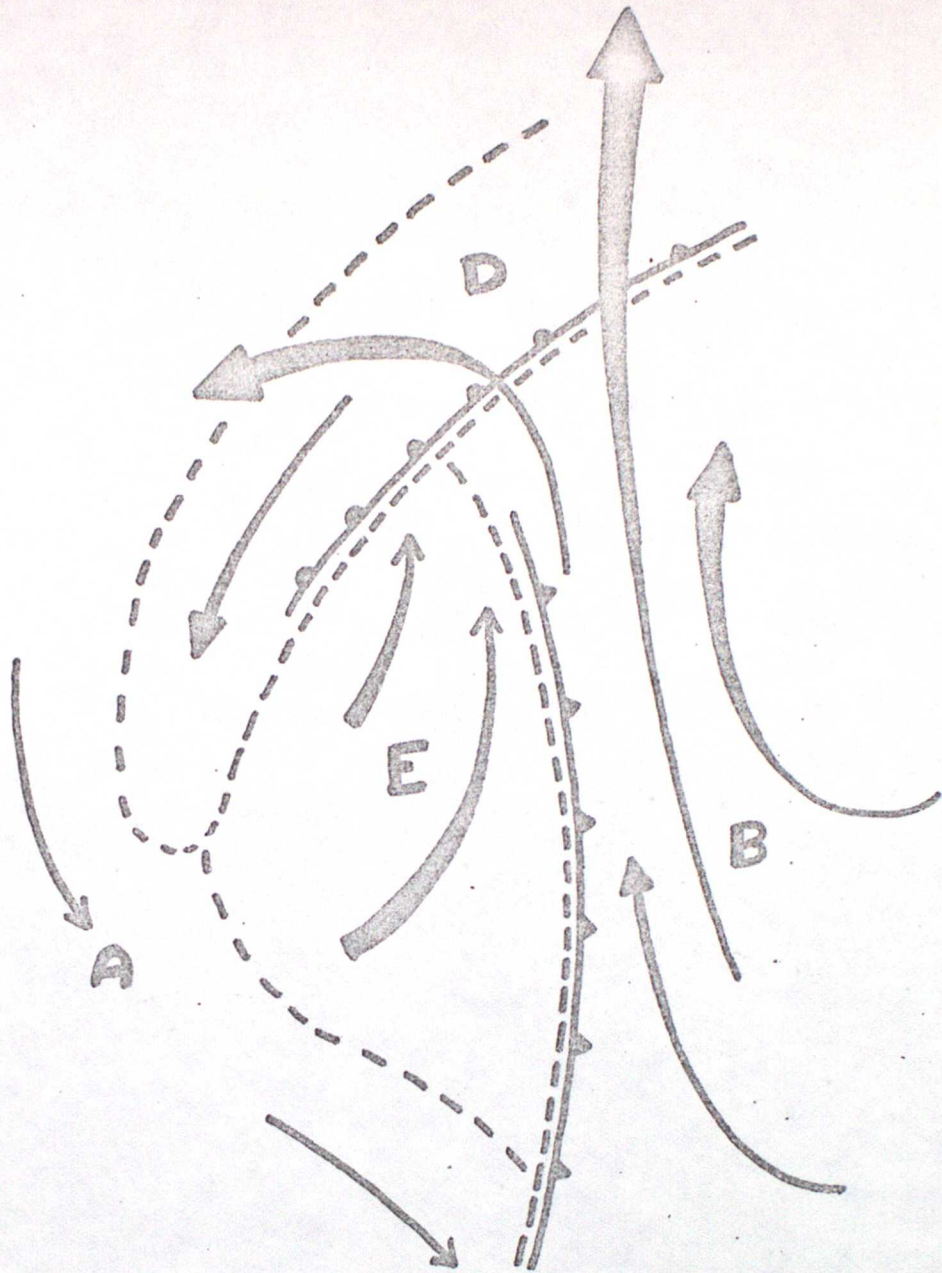


Fig 236

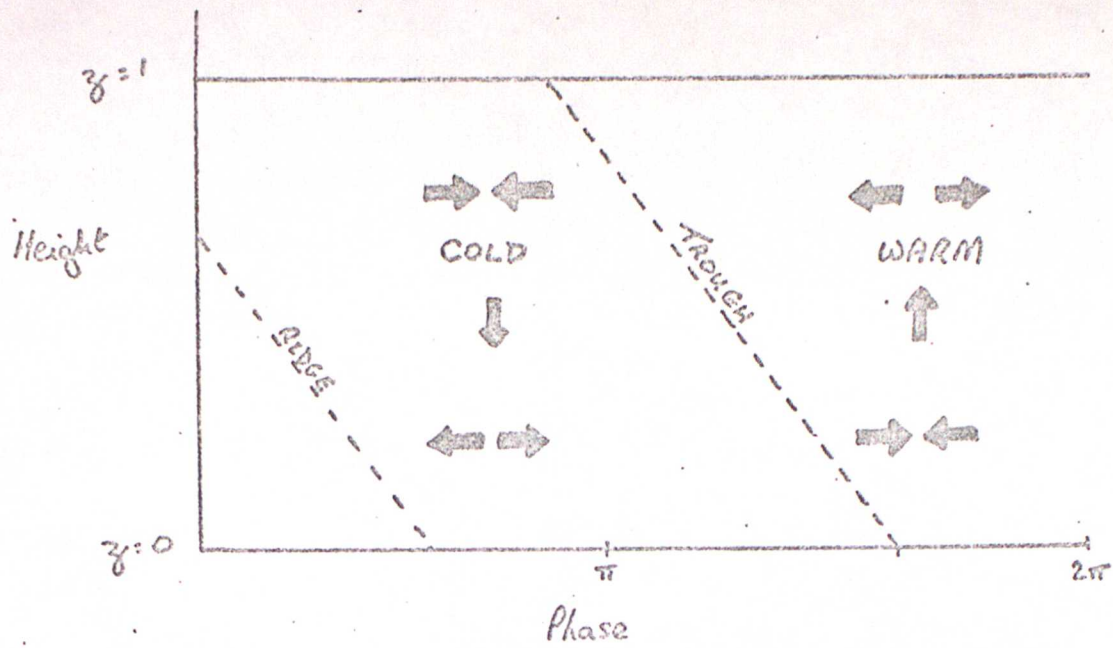


Fig 24

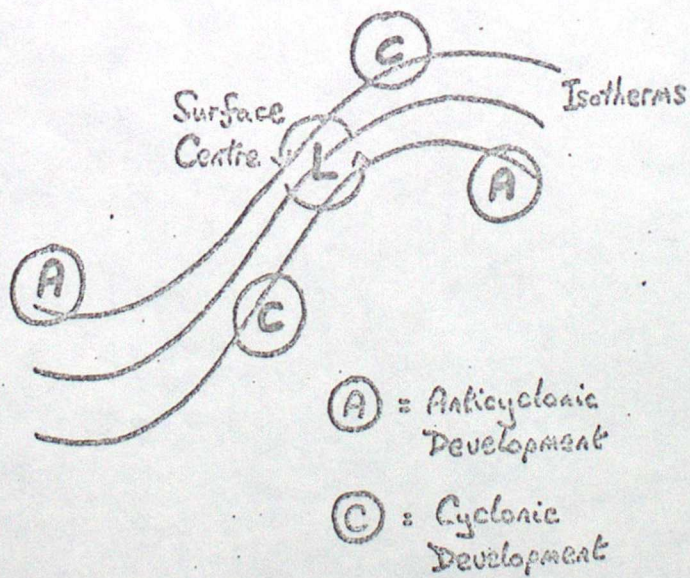


Fig 25